


Numerical modeling of droplet rim fragmentation by laser-pulse impact using a multiscale two-fluid approach

Georgia Nykteri * and Manolis Gavaises

School of Science and Technology, Department of Engineering, City University of London, Northampton Square, London EC1V 0HB, United Kingdom



(Received 29 September 2021; accepted 29 September 2022; published 20 October 2022)

In this paper, we examine the rim fragmentation of a millimeter-sized methyl-ethyl-ketone droplet imposed by the impact of different millijoule nanosecond laser beams that correspond to droplet propulsion velocity values between 1.76 and 5.09 m/s. The numerical investigation is conducted within a physically consistent and computationally efficient multiscale framework, using the Σ - Υ two-fluid model with dynamic local topology detection. Overall, the macroscopic droplet expansion and the obtained deforming shape show good agreement with the experimental observations. The influence of the laser beam energy on the droplet deformation and the evolution of the detached fragments from the rim is demonstrated. The physical mechanisms that determine the droplet expansion, including the expansion velocity and expansion rate, along with the effect of the surrounding air flow on the detached fragments, are addressed. Despite the visualization limitations inside the polydisperse cloud of fragments in the experimental results at higher laser energy, the evolution of fragments during the fragmentation process is quantified, and size distributions are obtained within the multiscale framework.

DOI: [10.1103/PhysRevFluids.7.103604](https://doi.org/10.1103/PhysRevFluids.7.103604)

I. INTRODUCTION

The droplet response to a laser-pulse impact is a polyparametric phenomenon, which remains of primary significance in varied state-of-the-art applications of both industrial and medical interest, including, among others, the extreme ultraviolet (EUV) light emission in lithography machines [1–4], the micromachining in the fabrication of photonic devices [5–7], and the laser ablation of biological tissues [8–11]. The absorption of the laser energy by the liquid droplet results in rapid and explosive phase-change phenomena, such as cavitation [12,13], vaporization [14–16], and plasma formation [17,18], observed in both transparent and liquid metal droplets. Because of the developed droplet dynamics after the laser-pulse impact, the droplet moves, deforms, and fragments into different patterns, dependent on the intensity of the applied laser beam energy and the material of the liquid droplet.

Authors of several experimental studies in the literature have investigated the laser-imposed fragmentation of a liquid droplet under different experimental configurations, which as a result, lead to different postimpact mechanisms. In the early literature, Kafalas and Herrmann [14] and Kafalas and Ferdinand [15] examined the explosive vaporization of single micron-sized water droplets imposed by a pulsed CO₂ laser with an energy of ~ 0.5 J per pulse. Later, Pinnick *et al.* [19] extended the explosive vaporization study for different liquids, e.g., for ethanol and diesel droplets, and observed similar fragmentation patterns with the water experiments for a pulsed CO₂ laser and comparable energy. Similar explosive response was also observed for micron-sized liquid

*georgia.nykteri.2@city.ac.uk

metal droplets in the experiments of Basko *et al.* [20] and Grigoryev *et al.* [21]; in this case, the picosecond laser pulse results in the development of a plasma state inside the droplet, while the development and propagation of a gigapascal pressure pulse inside the droplet triggers the subsequent violent fragmentation. More recently, Gonzalez Avila and Ohl [12] and Zeng *et al.* [22] studied a different explosive fragmentation mode, which develops as an outward widespread jetting from the droplet surface. Specifically, the laser impact onto a millimeter-sized water droplet with a cavitation bubble in the center imposes a laser-induced cavitation and bubble oscillations that penetrate the droplet surface; different fragmentation regimes were identified based on the dynamic pressure and the energy of the expanding bubble. In an attempt to control the deposition of the laser energy inside the droplet, Klein *et al.* [23–25] proposed the use of opaque liquid droplets, which restrict the energy absorption in a thin superficial layer on the illuminated side of the droplet. Specifically, Acid-Red-1 and Oil-Red-O solutions were utilized for water and methyl-ethyl-ketone (MEK) droplets, respectively, to investigate the droplet response to a broad range of laser energy between 1 and 420 mJ. Additionally, the similarities between the physical principles that govern the laser-induced droplet fragmentation and the fragmentation due to the mechanical impact of a droplet onto a solid surface [26] were highlighted; the impulsive acceleration of the droplet due to the laser impact can be correlated with the impulsive deceleration of the droplet when impacting the solid. Recently, Rao *et al.* [27] demonstrated the influence of the laser focus and energy on the resulting fragmentation of an array of micron-sized water and diesel droplets and identified a butterfly-type fragmentation pattern. Overall, the available experimental studies in the literature provide a thorough analysis of the droplet dynamics and the physical mechanisms that govern the subsequent fragmentation. However, due to the multiscale character of the fragmentation process, very few quantitative data are available regarding the produced fragments, for instance, in the high-resolution experimental visualizations of Klein *et al.* [25] and Rao *et al.* [27], which mainly concern moderate fragmentation regimes.

The hydrodynamics response of a liquid droplet to a laser-pulse impact is driven by the imposed recoil pressure on the droplet surface, as discussed in previous analytical and numerical studies in the literature. Specifically, the smooth particle hydrodynamics (SPH) method is commonly adopted for the investigation of liquid tin droplets, which are subject to high-energy picosecond laser beams. As depicted in the works of Grigoryev *et al.* [21] and Koukouvinis *et al.* [28], the SPH method can accurately predict the recoil pressure establishment and propagation inside the droplet shortly after the laser-pulse impact, the formation of dominant cavitation regions, and the early time explosive fragmentation using a given particle population. Concerning the commonly utilized Eulerian methods in droplet fragmentation simulations due to mechanical impact [29–31], Zeng *et al.* [22] employed the volume of fluids (VOF) method to study the cavitation-induced liquid jetting of a water droplet with a gas bubble in the center at initial conditions, impacted by a millijoule laser pulse. The coherent droplet interface and the formation of multiple outward liquid jets were accurately captured with the sharp interface method; however, the small-scaled fragments remain unresolved with the VOF method, which can result in significant loss of information in more violent fragmentation regimes with dominant polydisperse fragments. Gelderblom *et al.* [32] proposed the boundary integral (BI) method for the simulation of the laser-induced droplet deformation. The BI simulations precisely capture the droplet lateral and width deformation under different conditions; nevertheless, the effects of the surrounding air and the subsequent fragmentation of the elongated liquid sheet were excluded from the numerical modeling. Additionally, Gelderblom *et al.* [32] and Reijers *et al.* [33] presented an analytical solution for the developed flow fields inside the droplet, during the early times of the droplet response to the laser-pulse impact. In the analytical studies, they provided a further insight into the obtained recoil pressure and the resulting droplet dynamics that finally initiate the droplet deformation; however, the analysis is restricted to the early times before the droplet deformation becomes significant.

Following the numerical challenges imposed by the unrevealed laser-induced droplet fragmentation mechanisms, there is a gap in the up-to-date literature regarding a comprehensive numerical analysis that can capture both the early time droplet dynamics, evolving shortly after the laser-pulse

impact and the later time droplet fragmentation with consideration of all the produced multiscale fragments. In this paper, we propose the multiscale two-fluid approach, as developed by Nykteri *et al.* [34], to investigate the multiscale character of the later time droplet fragmentation. The numerical methodology has been previously validated against droplet fragmentation cases, driven by the high-speed mechanical impact on a solid surface [34]. In the present numerical simulations, the multiscale two-fluid approach employs a sharp interface method for the deforming and laterally expanding liquid droplet and a physically consistent subgrid scale modeling for the produced small-scaled fragments due to the rim breakup. In the conducted simulations, we do a thorough quantitative analysis of both the early and later time droplet dynamics with a viable computational cost. Specifically, significant information regarding the liquid droplet expansion into an elongated liquid sheet is revealed, including the droplet radial expansion velocity and the effect of the surrounding air. Additionally, the influence of the applied laser beam energy is demonstrated and shows good agreement with both the experimental observations of Klein *et al.* [25] and theory. Finally, an overview of the evolution of the population of the produced fragments is presented. The fragment dynamics, including the development of a cloud of fragments during the fragmentation process and the interaction between the detached fragments and the surrounding air under the impact of different beams, is highlighted, and size distributions are obtained.

In Sec. II are presented all the details of the numerical configuration for the conducted laser-induced droplet fragmentation simulations, including the problem formulation as described in the experimental studies of Klein *et al.* [23–25], the early time dynamics simulations, the governing equations of the multiscale two-fluid approach, and the later time dynamics simulations setup. Following, in Sec. III, the numerical investigations for the rim fragmentation of a liquid droplet, imposed by different intensity laser beams are discussed. The numerical results are compared with the experimental observations of Klein *et al.* [25] for the same examined conditions. Finally, the major conclusions are summarized in Sec. IV.

II. NUMERICAL MODELING

The fragmentation of a millimeter-sized MEK droplet imposed by the impact of a millijoule nanosecond laser pulse is investigated in this paper using numerical simulations. The MEK droplet with an initial radius of $R_0 = 0.9$ mm, density $\rho = 805$ kg/m³, kinematic viscosity $\nu = 0.53 \times 10^{-6}$ m²/s, and surface tension $\gamma = 0.025$ N/m lies in a nitrogen environment at ambient conditions ($p = 1$ atm, $T = 20$ °C). The laser-induced droplet dynamics concern two main stages, namely, the early time droplet response to the laser pulse and the later time droplet deformation and fragmentation. The early time droplet dynamics are discussed in Sec. II A based on the experimental investigations of Klein *et al.* [23–25], and a physically consistent numerical modeling is presented in Sec. II B, following the analytical model of Gelderblom *et al.* [32]; the obtained pressure and velocity fields inside the droplet are subsequently utilized for the initialization of the conducted numerical simulations that capture the later time phenomena. The numerical simulations of the later time droplet deformation and fragmentation are performed using the multiscale two-fluid approach, presented in Sec. II C. Details of the simulation setup are summarized in Sec. II D.

A. Problem formulation

The numerical modeling of the laser-induced droplet fragmentation is based on the problem formulation and the fundamental principles of the early and later time droplet dynamics, as introduced in the experimental studies of Klein *et al.* [23–25] and illustrated in Fig. 1.

The early time droplet dynamics in Figs. 1(i) and 1(ii) are characterized by the millijoule nanosecond laser pulse impact onto the droplet that results in local boiling on the superficial layer with thickness $\delta \ll R_0$ and the emission of a very small vapor mass in the surrounding air. The resulting recoil pressure on the droplet surface accelerates the droplet until it finally reaches a

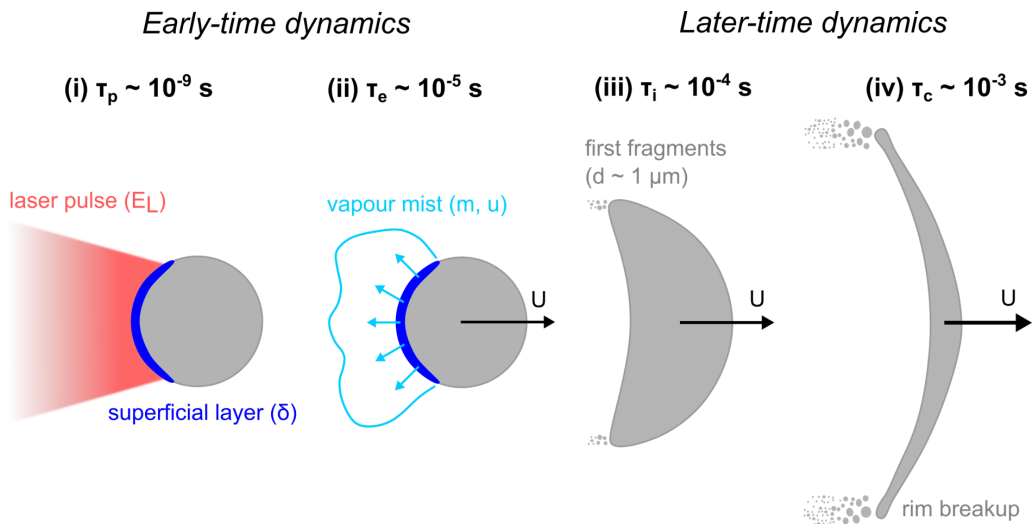


FIG. 1. Separation of timescales in the laser-induced droplet rim fragmentation problem. (i) A nanosecond laser pulse impacts the left side of the dyed droplet. (ii) The vaporized liquid mass on the superficial layer is ejected backwards. As a result, the droplet accelerates until it reaches a constant propulsion velocity U at the vapor expulsion time τ_e . (iii) The droplet propels and deforms at the inertial time τ_i . (iv) The surface tension and the extended fragmentation restrict the droplet lateral expansion at the capillary time τ_c .

constant propulsion velocity U , as expressed in the momentum conservation below:

$$mu = \rho R_0^3 U, \quad (1)$$

where m is the vaporized liquid mass on the superficial layer, u the velocity of the expelled vapor mass, ρ the liquid density, R_0 the initial droplet radius, and U the droplet propulsion velocity.

The primary parameter that determines the laser-induced droplet fragmentation, by establishing the propulsion velocity and thus the expansion rate of the droplet, is the Weber number of the propelled droplet, defined as

$$We = \frac{\rho R_0 U^2}{\gamma}, \quad (2)$$

where ρ is the liquid density, R_0 the initial droplet radius, U the droplet propulsion velocity, and γ the liquid surface tension.

During the later time droplet dynamics in Figs. 1(iii) and 1(iv), the deformation of the droplet surface dominates on the inertial timescale, defined as $\tau_i = R_0/U$, until eventually the droplet lateral expansion is restricted by the surface tension and the extended fragmentation on the capillary timescale, calculated as $\tau_c = \sqrt{\rho R_0^3/\gamma}$.

B. Early time dynamics and initial fields

The distinct separation of timescales in the laser-induced droplet fragmentation problem allows us to isolate the modeling of the early time droplet dynamics from the later time droplet deformation and fragmentation without introducing physical or numerical restrictions. Following this observation, Gelderblom *et al.* [32] provided a unified analytical model for all early time phenomena, starting from the laser-pulse impact onto the droplet for a duration τ_p , until the droplet propulsion with constant velocity on time τ_e , illustrated in Figs. 1(i) and 1(ii). The model concerns a pressure pulse with magnitude p_e applied on the droplet surface for a duration τ_e . Accordingly, the absolute impulse scale $p_e \tau_e$ imposes the droplet propulsion. The momentum conservation at time τ_e

is expressed as follows:

$$\int_0^{\tau_e} \int_A p_e e_z \cdot dA dt = \frac{4}{3} \pi \rho R_0^3 U, \quad (3)$$

where τ_e is the vapor expulsion time, A the droplet surface area, p_e the magnitude of the pressure pulse, ρ the liquid density, R_0 the initial droplet radius, and U the droplet propulsion velocity.

As derived from the assumptions of Gelderblom *et al.* [32] for an inviscid, irrotational, and incompressible flow, the pressure field inside the droplet at time τ_e is obtained from the solution of the Laplace equation:

$$\Delta p^* = 0, \quad (4)$$

for the nondimensional pressure field $p^* = p/p_e$. Subsequently, the velocity field inside the droplet at time τ_e is calculated from the momentum equation as

$$u = -\frac{\tau_e}{\rho} \nabla p, \quad (5)$$

while the nondimensional velocity field is obtained as $u^* = \rho R_0 u / p_e \tau_e$.

The pressure boundary condition of Eq. (4) refers to the original pressure pulse that is applied on the droplet surface and considers the dependence of the pulse shape on the angle θ , such that

$$p^*(r = 1, \theta) = f(\theta), \quad (6)$$

where the pulse $f(\theta)$ is proportional to the actual laser pulse that impacts onto the droplet surface in the conducted experiments of Klein *et al.* [23–25]. Therefore, Gelderblom *et al.* [32] suggested a Gaussian-shaped pressure pulse to remain consistent with the typically used Gaussian laser beam profiles in the experiments. The Gaussian-shaped pressure pulse is formulated as

$$f(\theta) = c e^{-\theta^2/2\sigma^2}, \quad (7)$$

where σ is the pulse width and

$$c = \frac{2\sqrt{2}}{\sigma \pi^{3/2} \exp(-2\sigma^2) [2\operatorname{erfi}(\sqrt{2}\sigma) - \operatorname{erfi}(\frac{i\pi+2\sigma^2}{\sqrt{2}\sigma}) - \operatorname{erfi}(\frac{-i\pi+2\sigma^2}{\sqrt{2}\sigma})]}.$$

In the experiments of Klein *et al.* [23], a laser beam profile with $\sigma = \pi/6$ is used; then $c = 0.825$.

In this numerical study, the previously presented analytical model for the early time droplet dynamics is adapted to be incorporated in the computational fluid dynamics (CFD) framework. Specifically, the MEK droplet is simulated as a 5° spherical wedge with one cell thickness in the azimuthal direction, using PIMPLEFOAM, a transient incompressible solver in OpenFOAM. As suggested in the analytical model, for times $t \leq \tau_e$, a pressure pulse is applied on the surface of the initially stagnant MEK droplet at ambient conditions. Correspondingly, the pressure pulse is set as the pressure boundary condition on the spherical wedge domain, given in dimensional form as

$$p(\theta) = p_e f(\theta) + p_{\text{atm}}. \quad (8)$$

Details of the numerical configuration for the simulation of the early time droplet dynamics are illustrated in Fig. 2(i).

At time $t = \tau_e$, the established pressure and velocity fields inside the droplet are calculated from the numerical simulations, as illustrated qualitatively in Fig. 2(ii). Later, the obtained flow fields are utilized for the initialization of the droplet in the conducted numerical simulations that initiate at time $t > \tau_e$ and capture the later time phenomena, as demonstrated in Sec. IID.

C. Later time dynamics and numerical method

The later time phenomena, illustrated in Figs. 1(iii)–1(iv), are governed by the deformation of the droplet into an elongated liquid sheet and the subsequent fragmentation of the droplet rim. The

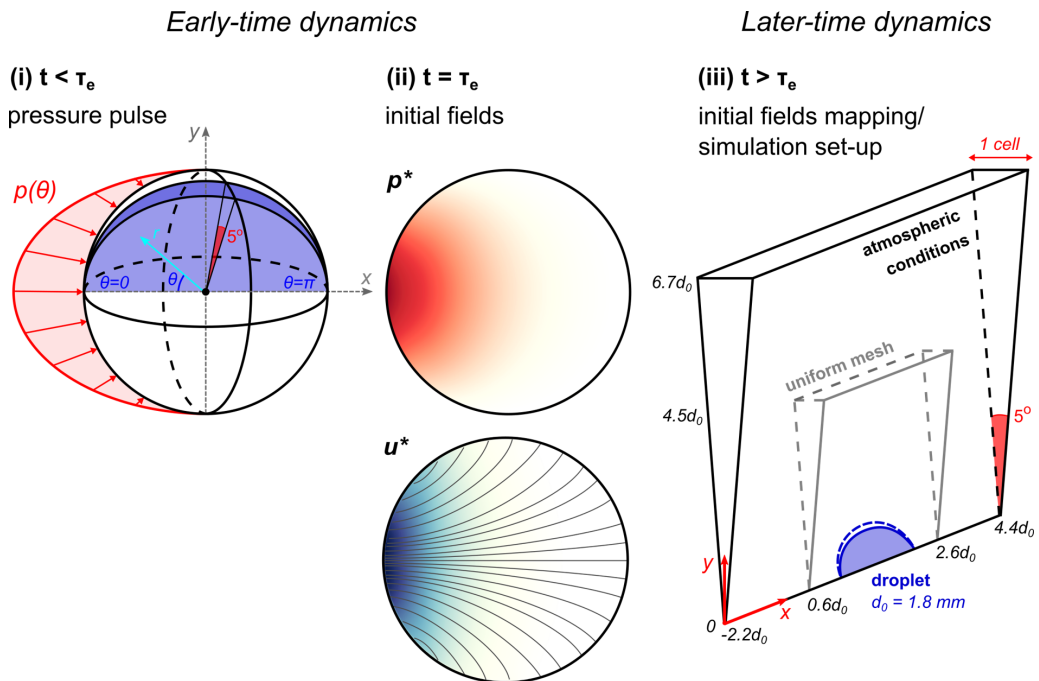


FIG. 2. Problem configuration and simulation setup. (i) For $t < \tau_e$, the axisymmetric pressure pulse $p(\theta)$ is applied on the droplet surface. (ii) At $t = \tau_e$, the initial pressure and velocity fields inside the droplet are obtained. (iii) The initial fields are mapped into the wedge geometry. For $t > \tau_e$, the droplet fragmentation is simulated using the multiscale two-fluid approach.

detached fragments form a polydisperse cloud of secondary droplets with diameters at least two orders of magnitude smaller than the initial droplet. Therefore, during the phenomenon, a flow field with dominant multiscale structures is developed, which imposes additional complexities in a full-scale and computationally efficient numerical analysis.

In this numerical study, the Σ - Y two-fluid model with dynamic local topology detection, introduced in the previous work of the authors [34], is utilized for the laser-induced droplet rim fragmentation simulations. The previously developed multiscale two-fluid approach provides a physically consistent and numerically stable multiscale framework for the investigation of all the scales involved in the laser-induced droplet fragmentation problem with a viable computational cost. A fundamental principle of the multiscale framework is the detection of different flow regimes based on advanced on-the-fly topological criteria and the application of the appropriate modeling approach for the local interfaces based on the dimensions of the underlying structures. The interface of the expanding but still coherent liquid sheet is fully resolved using the VOF sharp interface method [35,36]. On the contrary, the produced fragments, which are smaller than the local mesh resolution, are modeled within a diffuse interface approach. In this case, an additional transport equation for the interface surface area density Σ [37,38] is incorporated to model the unresolved subgrid scale phenomena and provides an estimation for the dimensions of the unresolved subgrid scale droplets.

The multiscale two-fluid approach has been implemented in OpenFOAM with further developments on the twoPhaseEulerFoam solver to introduce all the additional features of the multiscale framework, as described in detail in Ref. [34]. The numerical model consists of the same set of governing equations under both formulations, namely, the sharp and diffuse interface approaches,

with specific source terms to be activated and deactivated depending on the currently operating formulation of the solver, as summarized below.

1. Two-fluid model governing equations

The volume averaged conservation equations [39] governing the balance of mass, momentum, and energy for each continuum and interpenetrating fluid phase k are

$$\frac{\partial}{\partial t}(a_k \rho_k) + \nabla \cdot (a_k \rho_k u_k) = 0, \quad (9)$$

$$\frac{\partial}{\partial t}(a_k \rho_k u_k) + \nabla \cdot (a_k \rho_k u_k u_k) = -a_k \nabla p + \nabla \cdot (a_k \tau_k^{\text{eff}}) + a_k \rho_k g + \sum_{\substack{n=1 \\ n \neq k}}^2 M_{kn}, \quad (10)$$

$$\begin{aligned} & \frac{\partial}{\partial t}[a_k \rho_k (e_k + k_k)] + \nabla \cdot [a_k \rho_k (e_k + k_k) u_k] \\ &= -\nabla \cdot (a_k \mathbf{q}_k^{\text{eff}}) - \left[\frac{\partial a_k}{\partial t} p + \nabla \cdot (a_k u_k p) \right] + a_k \rho_k g \cdot u_k + \sum_{\substack{n=1 \\ n \neq k}}^2 E_{kn}, \end{aligned} \quad (11)$$

where α_k is the volume fraction, ρ_k the density, u_k the velocity, e_k the specific internal energy, k_k the specific kinetic energy fields for each phase, p the pressure field shared by both the liquid and gaseous phases, and g the acceleration of gravity. Viscous and turbulence effects are introduced with the effective stress tensor τ_k^{eff} , which accounts for the molecular viscosity and the Reynolds stress tensor based on Boussinesq's hypothesis [40] and the effective heat flux vector $\mathbf{q}_k^{\text{eff}}$, which corresponds to the laminar and turbulent thermal diffusivity. Here, M_{kn} represents the forces acting on the dispersed phase, depending on local topology; the surface tension force [41] is implemented under the sharp interface approach, while the aerodynamic drag force [42] is implemented under the diffuse interface approach. Also, E_{kn} demonstrates the heat transfer between the liquid and gaseous phases, irrespectively of the flow region.

2. Σ - Υ model transport equations

The transport equation for the liquid volume fraction in a compressible two-phase flow is given by

$$\frac{\partial a_l}{\partial t} + \nabla \cdot (a_l u_m) + v_{\text{topo}} \{ \nabla \cdot [a_l (1 - a_l) u_c] \} = a_l a_g \left(\frac{\psi_g}{\rho_g} - \frac{\psi_l}{\rho_l} \right) \frac{Dp}{Dt} + a_l \nabla \cdot u_m - (1 - v_{\text{topo}}) R_{a_l}, \quad (12)$$

where u_m is the velocity field of the liquid and gaseous mixture and ψ_l, ψ_g are the liquid and gaseous compressibility fields, respectively. Here, v_{topo} distinguishes the two different interface approaches by taking either the 0 or 1 value under a diffuse or sharp interface formulation, respectively. Interface sharpness is imposed by the artificial compression velocity u_c . Additional modifications in the governing equations for coupling the VOF method with the two-fluid framework are presented in detail in Ref. [34]. Finally, the term R_{a_l} accounts for the liquid dispersion induced by turbulent velocity fluctuations, which are important in dispersed flows and smaller scales [43,44].

The transport equation for the liquid-gas interface surface area density Σ [38] is given by

$$\frac{\partial \Sigma'}{\partial t} + \nabla \cdot (\Sigma' u_m) = (1 - v_{\text{topo}}) \left[-R_\Sigma + C_{\text{SGS}} \frac{\Sigma}{\tau_{\text{SGS}}} \left(1 - \frac{\Sigma}{\Sigma_{\text{SGS}}^*} \right) \right], \quad (13)$$

where the simultaneous existence of liquid and gas on the interface implies the presence of a minimum interface surface area density, such as $\Sigma = \Sigma' + \Sigma_{\text{min}}$, as shown by Chesnel *et al.* [45]. The term R_Σ represents the interface surface area diffusion due to turbulent velocity fluctuations

[44]. The subgrid scale source term, namely, the term $S_{SGS} = C_{SGS} \frac{\Sigma}{\tau_{SGS}} (1 - \frac{\Sigma}{\Sigma_{SGS}^*})$, accounts for all the unresolved physical mechanisms which are responsible for the local interface formation. The S_{SGS} term is a function of the constant adjustable parameter C_{SGS} , the characteristic timescale τ_{SGS} , and the critical interface surface area density Σ_{SGS}^* at an equilibrium state between interface production and destruction. Each modeled subgrid scale mechanism has either a positive or a negative contribution on the overall S_{SGS} term calculation. Specifically, a positive S_{SGS} term value corresponds to an increase of the local interface surface area and physically correlates with the evolution of the underlying subgrid scale droplets into smaller diameters, while a negative S_{SGS} term value describes a decrease of the local interface surface area due to the creation of subgrid scale droplets with larger diameters.

In these simulations of the laser-induced droplet fragmentation, the subgrid scale modeling is implemented for the small-scale fragments detached from the droplet rim with sizes below the local mesh resolution. The evolution of the droplet sizes inside the produced cloud of fragments depends on the aerodynamic conditions of the surrounding air and on the subgrid scale droplet interactions within the cloud. Therefore, the subgrid scale mechanisms that are considered for the local interface formation are the effects of turbulence, the subgrid scale droplet collision and coalescence, and the secondary breakup. The appropriate closure relations for each mechanism are based on models that are validated in the literature for similar flow conditions; the implemented subgrid scale models and their limitations are discussed in detail in Ref. [46].

The diameter of a subgrid scale fragment d_{Σ} is calculated as the equivalent diameter of a spherical particle which has the same volume-to-surface-area ratio as the examined computational cell, proposed by Chesnel *et al.* [45] as

$$d_{\Sigma} = \frac{6a_l(1 - a_l)}{\Sigma}, \quad (14)$$

where a_l represents the liquid volume fraction and Σ the total liquid gas interface surface area density, as calculated in Eq. (13).

3. Flow topology detection algorithm

The flow topology detection algorithm is implemented based on general and case-independent topological criteria that can be applicable in any flow field governed by multiscale structures, as described in detail in Ref. [34]. For these simulations of the laser-induced droplet fragmentation, the algorithm identifies instantaneous topological changes in the region around the droplet rim, where all the smaller-scaled structures are observed because of the rim breakup. Based on the sizes of the produced fragments, the algorithm evaluates and applies the most appropriate numerical formulation, namely, an interface capturing approach for the sufficiently large structures or a subgrid scale modeling for the unresolved fragments.

D. Later time simulation initialization and setup

The numerical simulations of the later time droplet deformation and fragmentation initiate at time $t > \tau_e$ with ambient atmospheric conditions, while the flow field inside the droplet is initialized based on the modeling of the early time phenomena in Sec. II B. The computational domain consists of a 5° wedge geometry with one cell thickness in the azimuthal direction and a mesh with a resolution of 200 cells per original droplet diameter around the area of interest is applied. Details of the initial configuration for the simulations of the later time phenomena are illustrated in Fig. 2(iii). Different Weber numbers in the range of 90–750 are examined with corresponding droplet propulsion velocities between 1.76 and 5.09 m/s. The simulation results are compared with the experimental observations of Klein *et al.* [25] for the same Weber numbers.

Regarding the numerical simulation setup, the spatial discretization is based on second-order accurate discretization schemes. Time stepping is performed adaptively during the simulation to respect the selected limit for the convective Courant-Friedrichs-Lewy condition of 0.2. The

thermodynamic closure of the system is achieved by implementing the stiffened gas equation of state, proposed by Ivings *et al.* [47], for the liquid phase and the ideal gas equation of the state for the gaseous phase. Concerning the turbulence modeling, a large-eddy simulations (LES) approximation is implemented with the one-equation SGS model of Lahey [48]. However, the utilized computational domain imposes limitations regarding the accurate capturing of the turbulent state, which corresponds to fully three-dimensionally (3D) developed phenomena. The simulations are initialized without turbulence in the flow field since the droplet acceleration at early times involves low velocities and Reynolds numbers $\sim 10^3$. Therefore, in the absence of developed turbulence at the initial conditions, the LES approximation can be applied in this geometry of one cell thickness in the azimuthal direction without significant modeling restrictions.

A crucial parameter for an accurate simulation of the later time droplet deformation and fragmentation is the initialization of the pressure and velocity fields inside the droplet at time $t = \tau_e$, as obtained from the early time simulations of Sec. II B. For a given Weber number, the droplet propulsion velocity is obtained from Eq. (2), and subsequently, the absolute impulse scale $p_e \tau_e$ can be calculated from Eq. (3), as introduced by Gelderblom *et al.* [32]:

$$p_e \tau_e = \frac{\rho R_0 U}{3}. \quad (15)$$

As shown in Eq. (15), different combinations of recoil pressure p_e and vapor expulsion time τ_e values determine different initialization sets (p_e, τ_e) for the same propulsion velocity U . Two conditions should apply for a valid expulsion time τ_e obtained for a known propulsion velocity: first, $\tau_e \gg \tau_p$ so that compressibility effects inside the droplet will not be significant, and thus, the modeling assumption of an incompressible flow will not be violated, and second, $\tau_e \ll \tau_i$ so that the applied pressure pulse will not have a macroscopic influence on the droplet spherical shape, and thus, the droplet will not deform yet.

In Appendix A, it is validated that, like the analytical solution of Gelderblom *et al.* [32], the droplet deformation obtained from the proposed later time simulations is dependent only on the absolute impulse scale and not on the individual p_e and τ_e values selected for a given propulsion velocity.

III. RESULTS AND DISCUSSION

The laser-induced rim fragmentation for a MEK droplet at $We = 330$ is presented in Figs. 3 and 4, comparing the simulation results with the experimental observations of Klein *et al.* [25]. Following the impact of the millijoule nanosecond laser pulse, the droplet has evolved into a thin liquid sheet surrounded by a cloud of fragments at time $0.056 \tau_c$ in Fig. 3(i). Subsequently, the liquid sheet expands further in the lateral direction, and at the same time, the observed rim breakup enhances the fragment cloud with polydisperse droplets of various diameters. The expanding liquid sheet is captured by the sharp interface formulation of the multiscale framework, while the detached fragments are subject to the subgrid scale modeling, as illustrated in Fig. 3(ii). Within the cloud of fragments, droplets with diameters between 0.09 and $9 \mu\text{m}$ are detected; the upper limit is correlated with the smallest structures that can be resolved with the sharp interface method for a local mesh resolution of 200 cells per initial diameter, and the lower limit corresponds to the spatial resolution of the utilized camera in the experiments. Overall, the numerically captured expanding sheet follows the deforming shape and the curvature observed in the experiments, while the modeled fragments are detected close to the liquid sheet during the early stages of fragmentation and move further backwards at later times. Moreover, the radial dependence of the sheet thickness, which is demonstrated in the experimental results in the front view in Fig. 4(i), is well predicted by the numerical simulations. Specifically, the maximum thickness is found in the center of the liquid sheet, and the minimum thickness is observed close to the rim. Consistent with the experimental observations of Klein *et al.* [25], the rim is captured as a slightly thicker border, as observed in the numerical results in Fig. 3(ii). At later times, a more uniform thickness is predicted along the

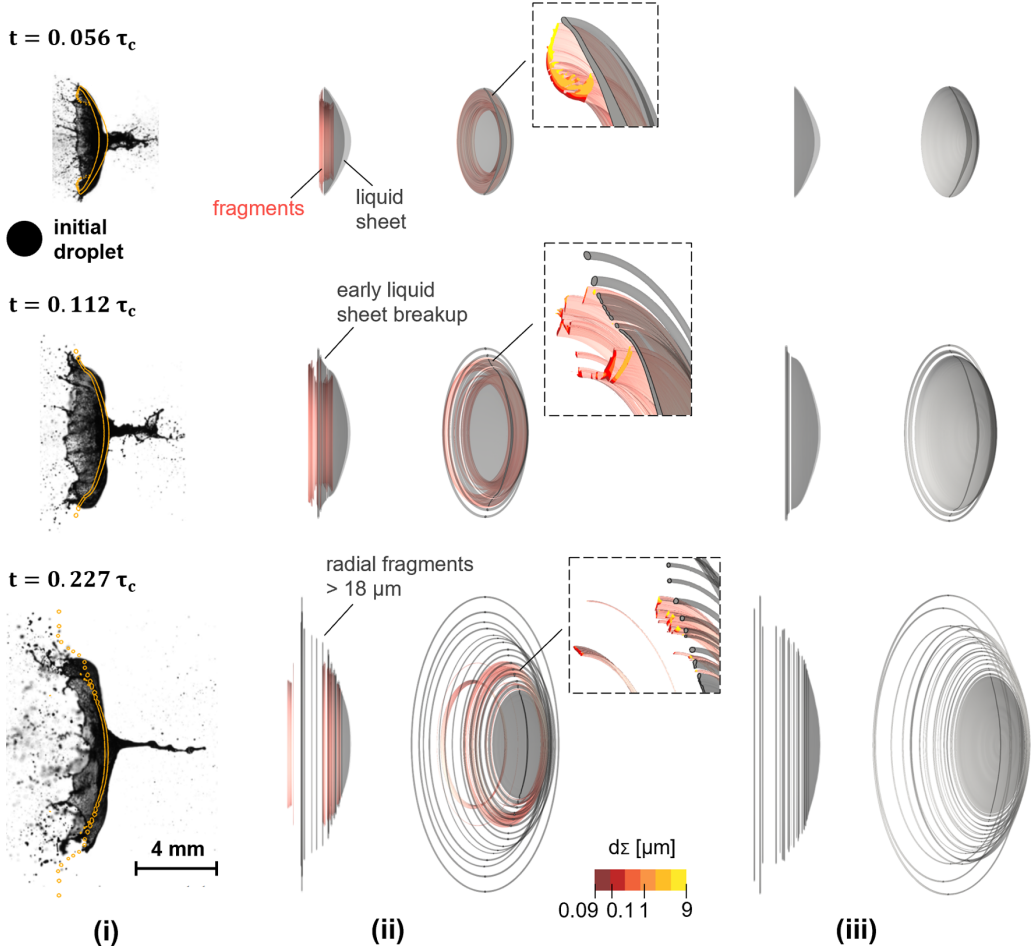


FIG. 3. Laser-induced droplet rim fragmentation at $We = 330$. (i) Comparison between the experimental visualizations of Klein *et al.* [25] in sideview and the isosurface of the liquid volume fraction at 10^{-3} , obtained with the multiscale two-fluid approach. (ii) Three-dimensional (3D) reconstructed results in sideview and 30° angle, using the multiscale two-fluid approach. The expanding liquid sheet is captured by the sharp interface formulation (in gray, the isosurface for liquid volume fraction at 0.5) and the detached fragments are captured by the diffuse interface formulation (in red, the isosurface for fragments $> 0.09 \mu\text{m}$). Zoomed-in view for the dimensions of the produced fragments after the rim breakup. (iii) 3D reconstructed results in sideview and 30° angle, using the volume of fluids (VOF) method. Isosurface of the liquid volume fraction at 0.5.

expanding sheet length, as displayed qualitatively in the liquid sheet isosurfaces in Fig. 3(ii) and extracted from the indicative calculations of the local thickness in Fig. 4(ii). Additional simulations are conducted using the VOF solver in OpenFOAM with the same initialization of the problem. The VOF method results, presented in Figs. 3(iii) and 4(iii), show good agreement with the respective results obtained with the multiscale two-fluid approach, regarding the capturing of the liquid sheet deformation; nevertheless, the VOF method excludes the subgrid scale information for the produced fragments.

Focusing on the predictions of the multiscale two-fluid approach in Figs. 3 and 4, at time $0.056 \tau_c$, which corresponds to the inertial time τ_i with dominant droplet deformation, the numerical results meet the experimental observations and accurately predict the macroscopic liquid sheet

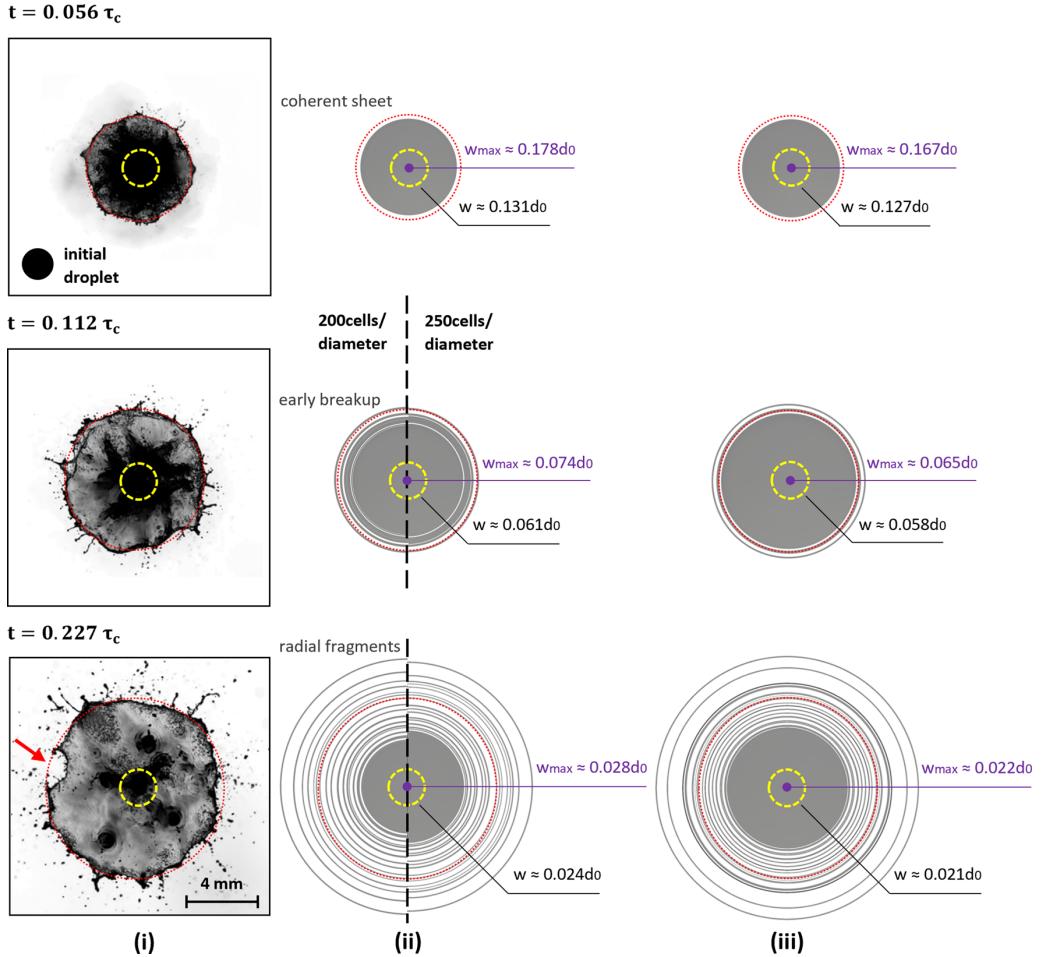


FIG. 4. Laser-induced droplet rim fragmentation at $We = 330$. (i) Experimental visualizations of Klein *et al.* [25] in front view. (ii) Three-dimensional (3D) reconstructed results in front view, using the multiscale two-fluid approach. The expanding liquid sheet, captured by the sharp interface formulation, is illustrated as the isosurface of the liquid volume fraction at 0.5 with a mesh resolution of 200 (left) and 250 (right) cells per initial droplet diameter. (iii) 3D reconstructed results in front view, using the volume of fluids (VOF) method. Isosurface of the liquid volume fraction at 0.5 with a mesh resolution of 200 cells per initial droplet diameter. The red circle defines the borders of the liquid sheet rim in the experimental results. The calculated thickness of the thin liquid sheet on the central line (in purple) and on the initial droplet radius (in yellow) is illustrated on the simulation results.

expansion. At the same time, a cloud of fragments that recirculate behind the expanding sheet is captured, with the largest droplets observed close to the rim.

Later, at time $0.112 \tau_c$, the liquid sheet thickness is reduced to $\sim 7\%$ of the initial droplet diameter. The numerical results satisfactorily follow the deforming shape of the thin liquid sheet and the lateral expansion, while smaller fragments are captured downstream. However, an early sheet breakup is observed close to the rim, where the local thickness of the liquid sheet is considerably reduced; a sheet breakup is not noticed in the experimental results at that time. Due to the axisymmetric geometry used in the numerical simulations the liquid sheet fragments detach in the form of concentric rings that move outwards, as illustrated in the 3D reconstructed numerical results

in Figs. 3(ii) and 4(ii). The multiscale two-fluid approach predicts a similar early sheet breakup even with a finer mesh of 250 cells per initial droplet diameter in Fig. 4(ii). In the VOF method results in Fig. 4(iii), the early sheet breakup is still present but developed to a smaller extent. The more pronounced early sheet breakup in the results of the multiscale model compared with the VOF results is related to the modeling of slip velocity effects; the relative velocity between the very thin liquid sheet and the surrounding air locally exceeds the value of 20 m/s around the rim, i.e., $\sim 6\times$ higher than the droplet propulsion velocity, and thus enhances the local sheet breakup. Overall, the early sheet breakup is a numerical limitation that originates from the utilized moderate mesh resolution which is found to be insufficient to accurately capture the significantly reduced sheet thickness around the rim at $0.112 \tau_c$. However, the implementation of a very fine uniform mesh will violate the fundamental principles of the multiscale two-fluid approach for computationally efficient simulations, i.e., the multiscale framework is based on a moderate uniform mesh resolution that accurately captures the large-scale structures and a subgrid scale modeling for the unresolved small-scale structures. Alternatively, the proposed multiscale framework should be extended to couple an adaptive mesh refinement (AMR) algorithm with the sharp interface formulation. The AMR algorithm would be able to resolve flow structures in the segregated flow regime that require significantly high resolution, such as the expanding liquid sheet, without an effect on the subgrid scale modeling formulation of the numerical model; this development is beyond the scope of our first numerical study on the laser-induced droplet fragmentation problem.

Following, at time $0.227 \tau_c$, these numerical limitations are observed as even more pronounced due to the significantly reduced thickness of the expanding liquid sheet. The length of the numerically captured coherent sheet is limited, while a trace of radial fragments follows the shape of the coherent elongated sheet, which is shown in the experimental visualizations. The successive detachment of radial fragments from the sheet rim is a numerical artifact, which is previously recognized in the BI simulations of Gelderblom *et al.* [32] during advanced stages of the fragmentation process. At the same time, the experimental results demonstrate the nucleation of holes on the liquid sheet as the major fragmentation mechanism. As illustrated in Fig. 4(i), the first holes are already detected along the rim at $0.227 \tau_c$, and thus, the assumption for an axisymmetric flow field is disrupted.

Considering that, in this paper, we attempt to provide numerical simulations for the laser-induced droplet fragmentation, the comparison between the experimental and numerical results in Figs. 3 and 4 is introduced as an investigation of the numerical capabilities of the proposed multiscale two-fluid approach. Overall, the observed numerical limitations, namely, the early sheet breakup and the loss of axisymmetry, arise only during advanced stages of the droplet fragmentation process. Therefore, the numerical simulations presented later in this paper focus on the droplet deformation and rim fragmentation before the numerical limitations become significant. Specifically, for the examined droplets and expansion rates, the numerical simulations are terminated at a selected final time that corresponds to the development of a liquid sheet with thickness $\sim 10\%$ of the initial droplet diameter on the central line; this is an acceptable limit before the early breakup and the loss of axisymmetry dominate. The validity of the utilized mesh resolution and geometry to accurately capture the underlying physical phenomena upon the laser-induced droplet deformation and fragmentation until the selected final time is discussed in Appendix B.

The fast jetting, which is shown in the experimental results in Fig. 3 to initiate from the center of the deforming droplet, is a result of the laser-matter interaction, as previously discussed by Klein *et al.* [25] and Reijers *et al.* [33]. The millijoule nanosecond laser pulse applied to the droplet surface results to strong shock waves and potential cavitation spots inside the droplet that can give rise to bubble collapse, interfacial instabilities, and finally, a fast jetting moving forward with a velocity larger than the propulsion velocity of the droplet. The absence of the fast jetting from the numerical results is not a limitation of the proposed numerical method but a result of the implemented modeling for the early time droplet dynamics. Specifically, this modeling approach of the early time dynamics does not account for the real laser pulse applied on the droplet for a duration τ_p . Instead, it provides a unified modeling solution for both early time dynamics phenomena, namely, the laser pulse impact and the resulting droplet propulsion, using a pressure pulse p_e and a duration

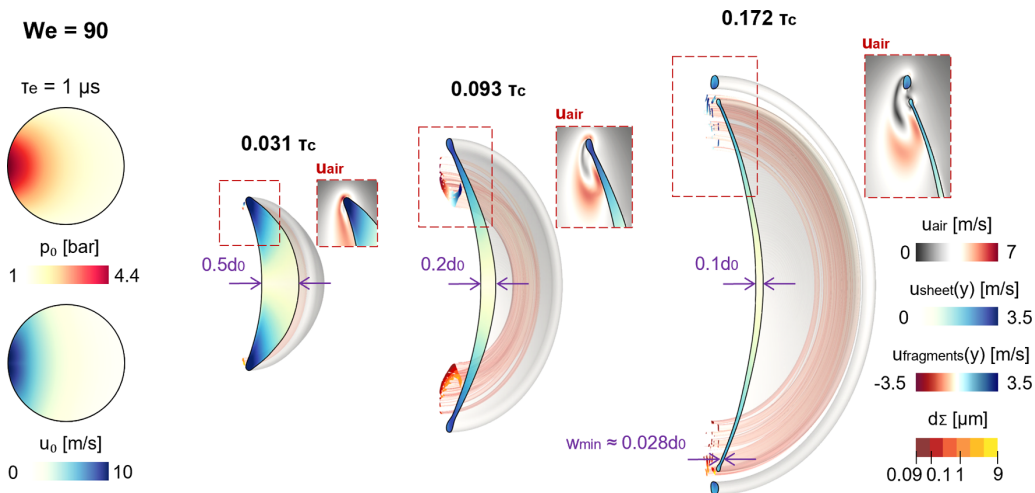


FIG. 5. Laser-induced droplet rim fragmentation at $We = 90$. Initial pressure and velocity fields inside the droplet, obtained for propulsion velocity $U = 1.76$ m/s and vapor expulsion time $\tau_e = 1$ μ s. Liquid sheet expansion velocity in the lateral direction, radial velocity (top) and dimensions (bottom) of the detached fragments for three time instances that correspond to liquid sheets with thicknesses 50, 20, and 10% of the initial droplet diameter. The air velocity field around the rim and the developed vortex are depicted in the side panels. The minimum captured thickness is illustrated at time $0.172 \tau_c$.

τ_e which are introduced for modeling purposes and do not correspond to the real laser intensity and duration. Alternatively, the fast jetting can be captured by avoiding this modeling of the early time phenomena and applying the real laser pulse to the droplet surface for the real impact duration τ_p . In this case, a compressible numerical model with advanced high-order numerical schemes should be implemented to capture the intense compressibility effects inside the droplet, and thus, the incompressibility assumption for the early time droplet dynamics will be no longer valid. However, considering the very small liquid mass injected, the investigation of the fast-jetting phenomenon remains beyond the scope of this paper.

The effect of the Weber number on the MEK droplet deformation and fragmentation is examined in Figs. 5–8 for Weber number values of 90, 170, 330, and 750 and the same width deformations corresponding to liquid sheets with thicknesses 50, 20, and 10% of the initial droplet diameter. Since the Weber number reflects the droplet expansion rate, which is set by the droplet propulsion, the examined width deformations are observed at very different times for each case. Already at the initial conditions, the strong impact of the Weber number is pronounced, resulting in significantly increased initial pressure and velocity magnitudes at higher Weber numbers. Specifically, for $We = 90$ in Fig. 5, the initial pressure and velocity fields inside the droplet, as calculated from the early time simulations to reach a propulsion velocity of 1.76 m/s, have a maximum value of 4.4 bar and 10 m/s, respectively. On the contrary, at $We = 750$ in Fig. 8, the stronger pressure pulse, applied on the droplet during the early time simulations for a propulsion velocity of 5.09 m/s, imposes initial pressure and velocity fields with the same profile but significantly increased maximum values up to 50.1 bar and 31 m/s, respectively.

Focusing on the early times of the droplet deformation at $We = 750$, due to the strong initial pressure kick, the formation of a low-pressure region inside the droplet is observed, which is related to the creation of cavitation bubbles. As highlighted in Fig. 8 at $0.01 \tau_c$, the developed low-pressure region is significantly small compared with the total mass of the deforming droplet, and thus, it does not affect the macroscopic droplet expansion. Therefore, a cavitation model has not been implemented in the multiscale framework for the examined conditions. Instead, a very small volume

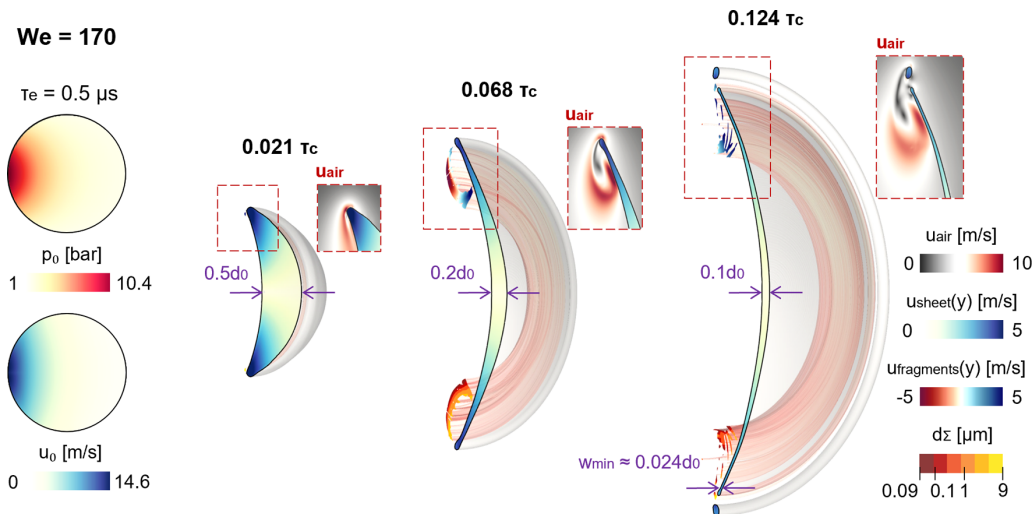


FIG. 6. Laser-induced droplet rim fragmentation at $We = 170$. Initial pressure and velocity fields inside the droplet, obtained for propulsion velocity $U = 2.42$ m/s and vapor expulsion time $\tau_e = 0.5 \mu\text{s}$. Liquid sheet expansion velocity in the lateral direction, radial velocity (top) and dimensions (bottom) of the detached fragments for three time instances that correspond to liquid sheets with thicknesses 50, 20, and 10% of the initial droplet diameter. The air velocity field around the rim and the developed vortex are depicted in the side panels. The minimum captured thickness is illustrated at time $0.124 \tau_c$.

fraction of air of the order of 10^{-6} , which corresponds to a typical nucleation volume fraction [49], is introduced in the initial droplet volume fraction. Under this assumption, the small gaseous volumes inside the droplet will expand after the significant pressure drop, causing expansion like those that would occur with cavitation. Subsequently, when the low-pressure region reaches the backside of the propelled droplet interface, the gaseous volumes collapse. Due to the minor breakup on the local interface, very few nanoscale droplets are captured by the numerical model at $0.035 \tau_c$; these droplets do not significantly influence the total population of the fragments.

During the laser-induced droplet deformation, the atmospheric pressure inside the droplet is rapidly recovered in a few microseconds, and a pressure distribution close to atmospheric conditions is stabilized before significant deformation is observed. Therefore, the droplet expansion is primarily governed by the radial component of the velocity $u_{\text{sheet}}(y)$, which shows maximum values on the expanding rim. More specifically, at early stages, until a liquid sheet with thickness $0.5d_0$ is developed in Figs. 5–8, the droplet deformation is the major phenomenon, while only a few droplets are detached from the rim. During these times, $u_{\text{sheet}}(y)$ induces the dominant liquid sheet radial expansion with the maximum values on the rim to be $\sim 2\times$ higher than the droplet propulsion velocity in each examined case. At later stages, when the liquid sheet thickness is reduced further than 50%, the rim fragmentation becomes significant, and hence, the droplet radial expansion is restricted. As a result, $u_{\text{sheet}}(y)$ gradually decreases over time; indicatively, $u_{\text{sheet}}(y)$ maximum values on the rim are decreased by ~ 17 and 11% between liquid sheets with thicknesses $0.5d_0$ and $0.2d_0$ at $We = 90$ and 750, respectively. At the final time, when a liquid sheet with thickness $0.1d_0$ is formed, the fragmentation rate is reduced, and less fragments are detached, as observed more evidently at lower Weber numbers in Figs. 5 and 6. Accordingly, the moderate fragmentation observed does not have a significant effect on the thin liquid sheet radial expansion, and $u_{\text{sheet}}(y)$ maximum values on the rim remain almost unchanged compared with earlier times.

Overall, the numerical results in Figs. 5–8 demonstrate that an increasing Weber number imposes a faster deformation of the initial spherical droplet into an elongated liquid sheet and an earlier breakup of the rim. Additionally, the effect of the Weber number on the shape of the deforming

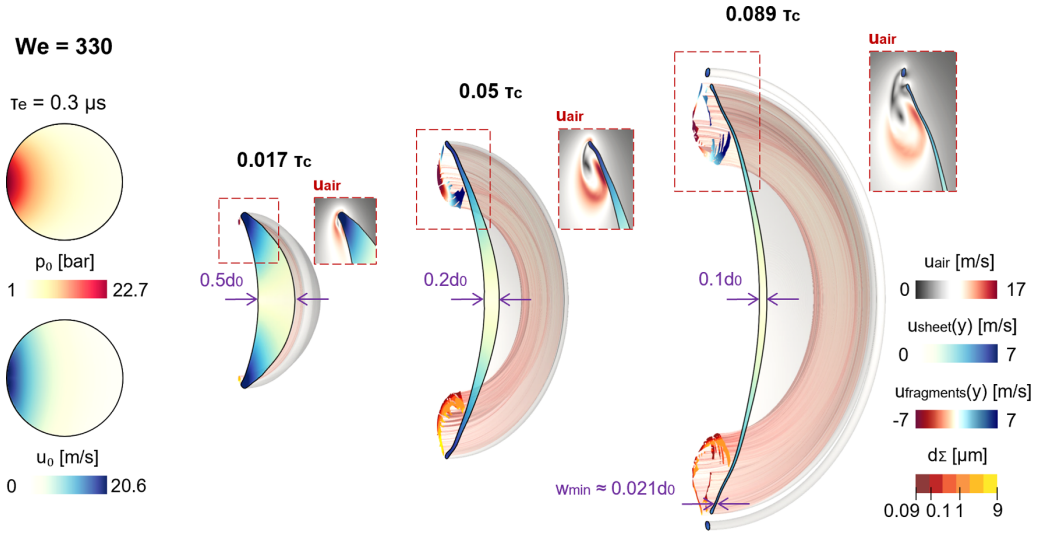


FIG. 7. Laser-induced droplet rim fragmentation at $We = 330$. Initial pressure and velocity fields inside the droplet, obtained for propulsion velocity $U = 3.37$ m/s and vapor expulsion time $\tau_e = 0.3 \mu\text{s}$. Liquid sheet expansion velocity in the lateral direction, radial velocity (top) and dimensions (bottom) of the detached fragments for three time instances that correspond to liquid sheets with thicknesses 50, 20, and 10% of the initial droplet diameter. The air velocity field around the rim and the developed vortex are depicted in the side panels. The minimum captured thickness is illustrated at time $0.089 \tau_e$.

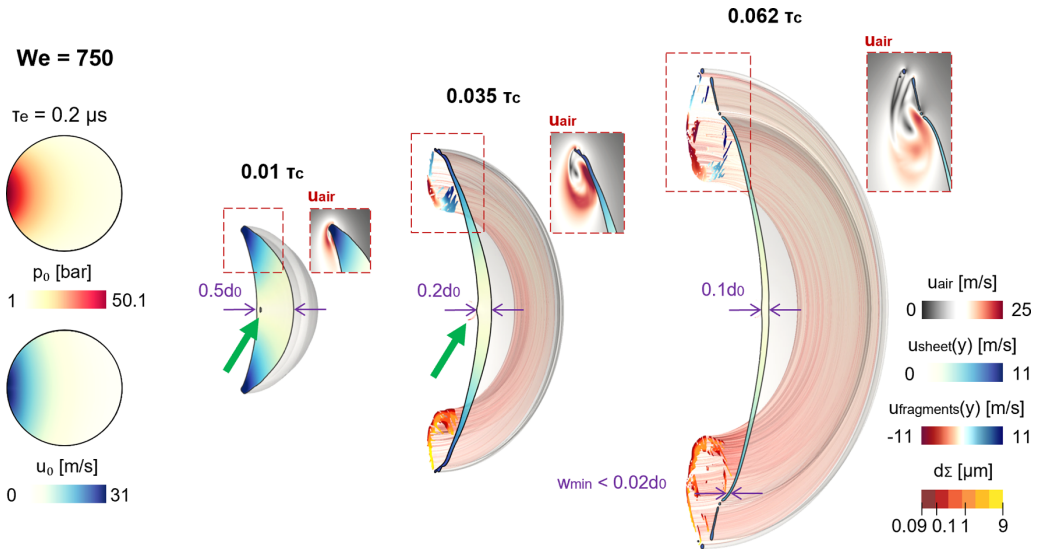


FIG. 8. Laser-induced droplet rim fragmentation at $We = 750$. Initial pressure and velocity fields inside the droplet, obtained for propulsion velocity $U = 5.09$ m/s and vapor expulsion time $\tau_e = 0.2 \mu\text{s}$. Liquid sheet expansion velocity in the lateral direction, radial velocity (top) and dimensions (bottom) of the detached fragments for three time instances that correspond to liquid sheets with thicknesses 50, 20, and 10% of the initial droplet diameter. The air velocity field around the rim and the developed vortex are depicted in the side panels. The minimum captured thickness is illustrated at time $0.062 \tau_e$. The arrows point to the minor low-pressure region and the very few created droplets after collapse.

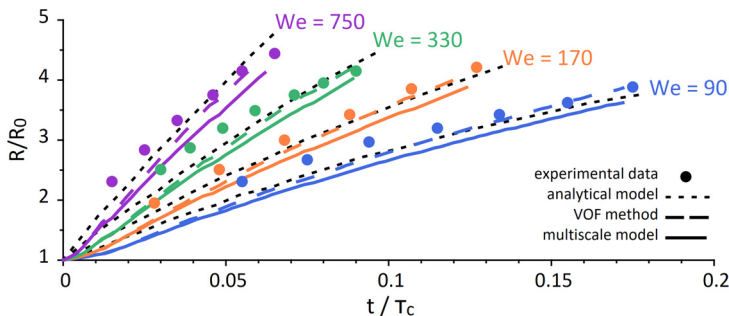


FIG. 9. Expansion of the liquid sheet radius because of the laser-induced droplet deformation at $We = 90$, 170, 330, and 750. Comparisons between the experimental observations of Klein *et al.* [25], the analytical model of Villermaux and Bossa [50], and the simulation results using the volume of fluids (VOF) method and the multiscale two-fluid approach until a liquid sheet with thickness 10% of the initial droplet diameter is formed.

liquid sheet concerning both the lateral expansion and the radial distribution of the thickness is highlighted. Specifically, during the early stages of deformation, the droplet shows an almost identical shape in the four examined cases for the same thickness reduction by 50%; the examined deformation is observed at different times for each case in accordance with the Weber number dependent expansion rates. However, at later times, when a thin liquid sheet is already formed, a higher Weber number leads to an increased lateral expansion and thus a more uniform thickness distribution for the same width deformation on the central line. Indicatively, for a liquid sheet with thickness $0.2d_0$, the lateral sheet expansion is increased by $\sim 7\%$ at $We = 330$ and by 13% at $We = 750$ compared with the predicted expansion at $We = 90$ for the same thickness.

Alongside the liquid sheet lateral expansion, the rim fragmentation becomes significant over time, as observed in Figs. 5–8. For a liquid sheet with thickness $0.5d_0$, the first microscaled fragments are detached from the rim, while at later times, when the liquid sheet thickness is reduced to $0.2d_0$, the dominance of the rim fragmentation is pronounced with an extended cloud of fragments to be developed in each examined Weber number case. On average, the largest fragments with diameters $> 1 \mu\text{m}$ are detected close to the rim, and the smallest scales are observed at the edges of the polydisperse cloud. On the contrary, at the final time, the fragmentation process is weakened. Then a significantly limited cloud of fragments is observed at lower Weber numbers in Figs. 5 and 6, while at higher Weber numbers in Figs. 7 and 8, the cloud of fragments remains extended, but on average, less and smaller-scaled fragments $< 3 \mu\text{m}$ are detached. During the evolution of the rim fragmentation, the newly formed fragments are detached from the rim with radial velocities $u_{\text{fragments}}(y)$ comparable with the radial velocity of the rim $u_{\text{sheet}}(y)$ at the time of breakup, as also observed in the experimental study of Klein *et al.* [25]. Afterwards, the fragments are subject to a recirculation behind the liquid sheet, driven by the moving vortex that is created because of the interaction between the propelled and expanding liquid sheet and the surrounding air. For a liquid sheet with thickness $0.2d_0$, the developed flow vorticity is found to be intense in all cases illustrated in Fig. 5–8, with local air velocity values $> 2 \times$ higher than the velocities of the fragments. During later stages, the flow vorticity becomes less significant; however, it still influences the increasing cloud of fragments at higher Weber numbers, as shown at $0.089 \tau_c$ and $0.062 \tau_c$ in Figs. 7 and 8, respectively.

A quantitative comparison between the experimental observations of Klein *et al.* [25], the analytical model of Villermaux and Bossa [50], and the simulation results using the VOF method and the multiscale two-fluid approach is presented in Fig. 9, examining the droplet radial expansion under the Weber numbers examined before. In the numerical simulations, the droplet expansion is considered until a thin liquid sheet with maximum thickness 10% of the initial droplet diameter is formed. Overall, the numerical results capture the strong dependence of the droplet expansion rate

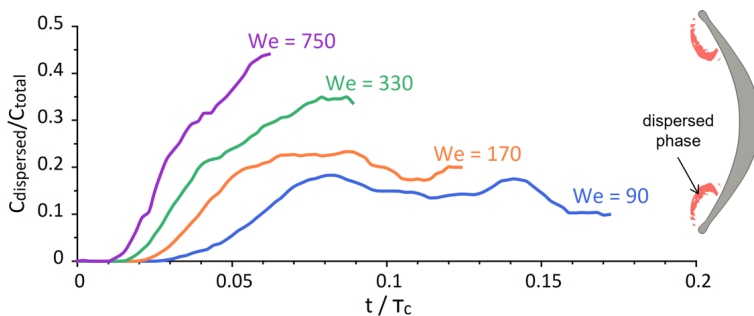


FIG. 10. Volume concentration of the dispersed region over the total volume of the liquid phase for the laser-induced droplet fragmentation at $We = 90, 170, 330,$ and 750 .

on the Weber number and satisfactorily follow the experimental observations. Better agreement between the numerical and experimental results is obtained at the later stages of the droplet expansion process, as similarly observed for the analytical solution. However, in contrast with the analytical model [50], the conducted numerical simulations can accurately capture all stages of the droplet deformation from a flattened back side to an elongated liquid sheet; thus, the small deviation between the numerical and experimental results at early times is not a limitation of the numerical model. Similarly, in the study of Gelderblom *et al.* [32], the BI simulation results of a water droplet radial expansion slightly deviate from the experimental observations, especially at early times. Considering that the BI simulations use the same early time initialization of the laser-induced droplet fragmentation problem as this numerical study, the small delay of the droplet radial expansion at early times can be related to the early time simulations and the lack of the impulsive effect of the laser-matter interaction in the modeling of early time dynamics. With respect to the capability of the numerical methods to accurately capture the overall droplet deformation and radial expansion over time, the VOF method results precisely follow the predictions of both the analytical model and the experiments during the advanced stages of droplet expansion, while the multiscale two-fluid approach results capture the phenomenon with on average a small delay of maximum 5% compared with the calculations with the VOF method. The slightly delayed expansion, observed with the two different numerical methods, can be related to the subgrid scale modeling, which is performed within the multiscale two-fluid approach and accounts for the produced fragments due to the rim breakup. Under the multiscale framework, a part of the deformation energy that would be utilized for the droplet radial expansion is now employed for the development of fragments. However, as depicted in Fig. 10, the volume concentration of the modeled fragments over the total volume of the liquid phase increases significantly at higher Weber numbers. Thus, the production of fragments is not negligible during the droplet expansion and the resulting rim fragmentation. At lower Weber numbers, the concentration of fragments relatively stabilizes during the rim fragmentation evolution, while with an increasing Weber number, the fragment population is continuously enhanced over time and even exceeds 40% of the total liquid volume at the later stages of rim fragmentation for the highest examined Weber number of 750.

An overview of the evolution of the produced fragments inside the polydisperse cloud is depicted in Fig. 11, where the volume concentrations of three classes of fragments with diameters $d_\Sigma > 1 \mu\text{m}$, $0.5 \mu\text{m} < d_\Sigma < 1 \mu\text{m}$, and $0.09 \mu\text{m} < d_\Sigma < 0.5 \mu\text{m}$ are presented for a MEK droplet at $We = 90, 170, 330,$ and 750 over the total volume of the dispersed region. Upon the initiation of the laser-induced droplet rim fragmentation, only large-scaled fragments of the first class $> 1 \mu\text{m}$ are detected for each examined Weber number case; these correspond to the first detached fragments from the rim. Subsequently, more fragments are detached from the rim that enhance the fragment population, while at the same time, the previously formed fragments interact with each other and develop further inside the polydisperse cloud. The modeled subgrid scale fragment

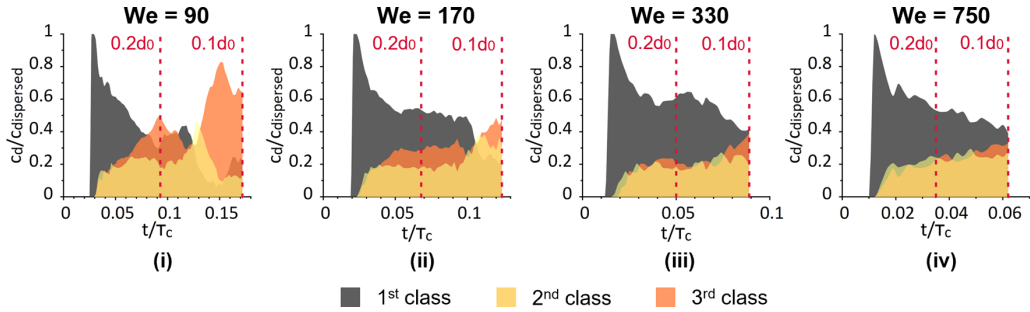


FIG. 11. Volume concentration of three classes of fragments with diameters $d_\Sigma > 1 \mu\text{m}$ (first class), $0.5 \mu\text{m} < d_\Sigma < 1 \mu\text{m}$ (second class), and $0.09 \mu\text{m} < d_\Sigma < 0.5 \mu\text{m}$ (third class) at $We = 90, 170, 330,$ and 750 over the total volume of the dispersed region. The vertical lines correspond to liquid sheets with thicknesses 20% and 10% of the initial droplet diameter.

interactions, namely, the flow turbulence, the droplet collision and coalescence, and the secondary breakup effects, are driven by the developed flow vorticity. Specifically, the moving vortex, which forms behind the expanding liquid sheet, enhances the local mixing and the slip effects between the newly formed microscaled fragments of the first class and the surrounding air and leads to further breakup of the fragments inside the cloud. On average, fragments of the second and third classes with diameters $< 1 \mu\text{m}$ are not directly detached from the rim and are created at a second stage due to the droplet interactions inside the cloud.

During later stages, when a liquid sheet with thickness $0.2d_0$ is formed, the rim fragmentation process is fully developed, and an extended cloud of fragments is created downstream, as previously illustrated in Figs. 5–8. Then the effect of the Weber number on the rim fragmentation rate and the produced fragment population is pronounced. Specifically, for a liquid sheet with thickness $0.2d_0$ at $We = 90$ in Fig. 11(i), the population of large-scaled fragments of the first class is significantly decreased, which can be related to the stabilization of the fragmentation mechanism and the reduction of newly formed fragments, as shown in Fig. 10. Instead, smaller-scaled fragments become dominant since the existing fragments inside the cloud are subject to further breakup driven by the intense flow vorticity. On the contrary, for a liquid sheet with thickness $0.2d_0$ and higher Weber numbers in Figs. 11(ii)–11(iv), the first class of fragments remains dominant, following the positive fragmentation rate and the continuous enhancement of the dispersed cloud with newly formed fragments, as depicted in Fig. 10. At the same time, smaller scales become significant because of the fragment interactions within the recirculating cloud; at $We = 170$, the third class of fragments is more noticeable, while at $We = 330$ and 750 , the population of fragments $< 1 \mu\text{m}$ is more balanced. Therefore, as observed for the examined cases, with increasing Weber number, the intensity of the rim fragmentation mechanism is also increased and dominates over the interactions of the fragments and breakup imposed by the developed flow vorticity.

During advanced stages of the rim fragmentation process for a liquid sheet with thickness $\sim 0.1d_0$, the fragmentation rate weakens over time, even at higher Weber number cases of values 330 and 750, as depicted in Fig. 10. This is reflected in a less violent rim fragmentation and the creation of less and smaller newly formed fragments, as previously discussed in Figs. 5–8. Consequently, smaller-scaled fragments $< 1 \mu\text{m}$ gradually dominate the fragment population and become even more significant at lower Weber numbers. Eventually, at the final time of the examined rim fragmentation, the predominant presence of the small-scaled fragments of the second and third classes, i.e., fragments $< 1 \mu\text{m}$, is highlighted in the probability density functions (PDFs) of the fragment sizes in Fig. 12. The fragments sizes follow an exponential decrease in all Weber number cases, as indicatively plotted against the PDFs in Fig. 12, with the largest captured fragments to be $\sim 3 \mu\text{m}$. At lower Weber numbers in Figs. 12(i) and 12(ii), $\sim 80\%$ of the total fragment

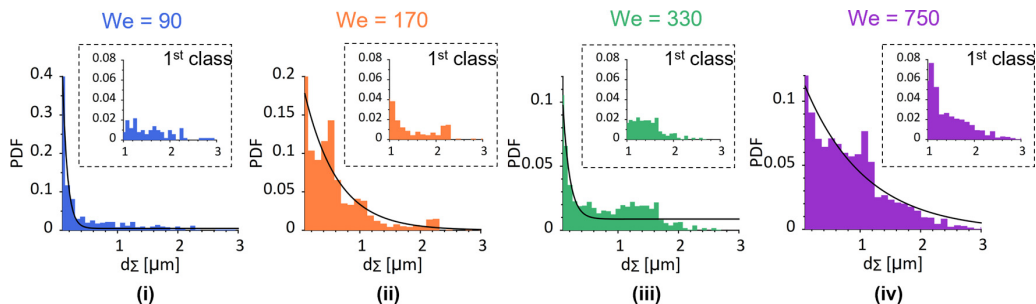


FIG. 12. Probability density functions (PDFs) of the fragment sizes at $We = 90, 170, 330,$ and 750 at the final time for a liquid sheet with thickness 10% of the initial droplet diameter. Zoomed-in view for the PDFs of the first class of fragments with diameters $d_\Sigma > 1 \mu\text{m}$. An exponential distribution is indicatively plotted against the PDF in each case.

population consists of fragments $< 1 \mu\text{m}$; the pronounced dominance of small-scaled fragments comes in agreement with the previous observations of a limited number of newly formed fragments, as depicted in the stabilized volume concentration of the dispersed cloud in Fig. 10. On the contrary, at higher Weber numbers in Figs. 12(iii) and 12(iv), fragments $< 1 \mu\text{m}$ remain dominant in the population by 60%; however, the significant presence of larger-scaled fragments indicates that, despite the attenuation of the fragmentation mechanism, the rim breakup continues to play a major role. Finally, a mesh convergence investigation for the calculated fragment populations is presented in Appendix C.

IV. CONCLUSIONS

The laser-induced droplet rim fragmentation for a millimeter-sized MEK droplet has been investigated in this numerical study, examining a range of Weber numbers between 90 and 750 for the propelled droplet. The problem is characterized by the early time droplet dynamics, imposed by the millijoule nanosecond laser-pulse impact and the subsequent response of the droplet until it reaches a constant propulsion velocity, and the later time droplet dynamics, governed by the droplet deformation into an elongated liquid sheet and the resulting rim breakup. The early time droplet dynamics were simulated within the CFD framework based on the analytical model of Gelderblom *et al.* [32], and the developed flow fields inside the droplet were obtained. Subsequently, the later time droplet dynamics were simulated using the multiscale two-fluid approach, which allowed for the consideration of all the scales involved with a viable computational cost. Specifically, the radial expansion of the developed liquid sheet was resolved by the local mesh resolution, using the VOF sharp interface method, while the produced fragments due to the rim breakup were modeled under the diffuse interface approach with consideration of the significant subgrid scale phenomena inside the cloud of fragments. The simulation results showed a good agreement with the experimental observations of Klein *et al.* [25] with respect to the shape and the expansion of the elongated liquid sheet and the development of a polydisperse cloud of fragments, until a selected final time before the numerical limitations and the nucleation of holes on the liquid sheet surface become significant.

The numerical simulations demonstrated the influence of the laser beam energy on the initial flow fields inside the droplet and the subsequent droplet deformation and rim fragmentation; these observations have a general interest for different droplets and conditions but the same droplet Weber number. Specifically, with increasing Weber numbers, a higher expansion rate, a more uniform liquid sheet thickness, and a more extended cloud of fragments at the later stages of fragmentation were captured. Quantitative information for the radial velocity fields, which are responsible for the droplet expansion, were provided, showing maximum values on the rim. Additionally, during the liquid sheet expansion, the formation of a moving vortex behind the rim was identified because of

the interaction between the expanding liquid sheet and the surrounding air; thus, the vortical flow creates a recirculation region for the produced fragments. Finally, an overview of the evolution of the population of the fragments during the droplet rim fragmentation and the sizes distributions at the final time of the phenomenon were presented. Overall, larger-scale fragments were detached from the rim at the early stages of fragmentation, while smaller fragments $< 1 \mu\text{m}$ dominated at the later stages because of the further breakup of the secondary droplets inside the cloud and the attenuation of the fragmentation mechanism over time. However, with increasing Weber number, droplets $> 1 \mu\text{m}$ remain significant even at the final times.

Further development of the proposed multiscale two-fluid approach to incorporate an AMR algorithm and phase-change phenomena, namely, a cavitation and vaporization model, will provide a valuable numerical model to investigate a broader range of unsteady fragmentation problems and obtain insight into the sizes of the produced fragments that is not easily accessible from the experimental observations. Examples of fragmentation cases of interest in the literature to date include the violent laser-induced droplet fragmentation in biofuels [51] and screen printing inks [52], the explosive droplet fragmentation [22] and the surface jet breakup [53] by laser-induced cavitation bubbles, and the breakup of laser-induced jets in needle-free medical injections [54], among others.

ACKNOWLEDGMENTS

This paper was supported by the European Union Horizon-2020 Research and Innovation Programme (Haos Project), Grant Agreement No. 675676. Additional funding has been received by the UK's Engineering and Physical Sciences Research Council (EPSRC) through Grant No. EP/K020846/1. The authors gratefully acknowledge the valuable help and fruitful discussions with Dr. Pierre Chantelot and Professor Detlef Lohse about the physics of the laser-induced droplet deformation and fragmentation and the initialization of the performed simulations upon the early investigations of this paper.

APPENDIX A: LATER TIME SIMULATION INITIALIZATION AND EFFECT ON DROPLET DEFORMATION RATE

The absolute impulse scale $p_e \tau_e$ defines the later time droplet dynamics and the resulting droplet deformation for a given propulsion velocity. However, as shown in Eq. (15), for a specified impulse scale $p_e \tau_e$, different initialization sets (p_e, τ_e) can be derived and equivalently used for the initialization of the later time simulations at $t = \tau_e$. In Fig. 13, the droplet radial expansion and width reduction is demonstrated for the examined MEK droplet at Weber numbers 90, 170, 330, and 750 using three different initialization sets for each Weber number. Overall, the droplet deformation rate remains almost unaffected by the different initialization sets of the same problem, like the previous observations of Gelderblom *et al.* [32].

APPENDIX B: VALIDITY OF NUMERICAL MODEL: MESH RESOLUTION AND GEOMETRY

The capability of the proposed multiscale two-fluid approach to accurately capture the laser-induced droplet deformation and rim fragmentation until the selected final time of the numerical simulations is discussed below; the selected final time corresponds to the development of a liquid sheet with thickness 10% of the initial droplet diameter on the central line. In this investigation, we focus on the two major aspects that can raise limitations in the conducted simulations, namely, the convergence of the numerical solution and the accuracy of the axisymmetric assumption.

1. Mesh convergence investigation

The droplet response to the laser pulse impact is related to three main macroscopic physical phenomena: the droplet propulsion, deformation, and fragmentation. Each phenomenon is investigated

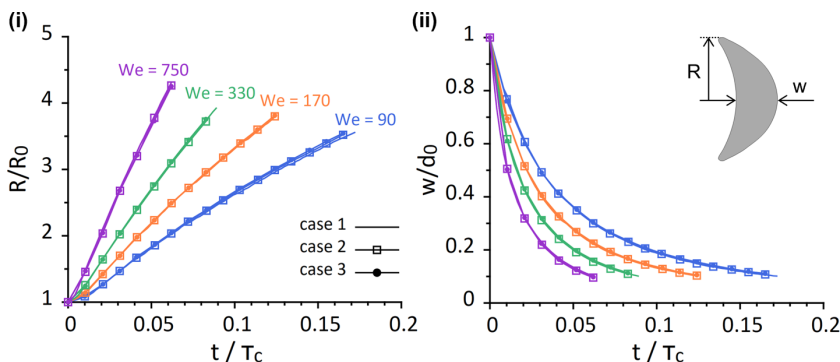


FIG. 13. Evolution of the laser-induced droplet deformation at $We = 90, 170, 330,$ and 750 . (i) Droplet radius expansion and (ii) droplet width reduction for three different initialization sets, namely, the same impulse scale $p_e \tau_c$ but different individual p_e and τ_e values, for each examined propulsion velocity and until a liquid sheet with thickness 10% of the initial droplet diameter is formed.

below with respect to the convergence of the numerical solution for a MEK droplet at $We = 90, 170, 330,$ and 750 using three different mesh resolution of 150, 200, and 250 cells per initial droplet diameter until the selected final time of the numerical simulations.

(1) The center-of-mass properties in the axial direction in Fig. 14 depict the droplet propulsion. Both the axial position and the axial velocity of the center-of-mass are accurately captured by all the applied mesh resolutions. The small decrease of the axial center-of-mass velocity over time is observed as more rapid with an increasing Weber number because of the surrounding air that becomes more significant at higher propulsion velocities, i.e., the center-of-mass velocity is reduced by $\sim 10\%$ and 13% at the final time for $We = 90$ and 750 , respectively.

(2) The droplet radial and axial deformation is illustrated in Fig. 15; the measurements of the droplet radial expansion converge with an increasing mesh resolution, while very good agreement is demonstrated for the measurements of the droplet axial deformation irrespective of the utilized mesh.

(3) The evolution of the rim fragmentation is investigated in Fig. 16, illustrating the volume concentration of the dispersed phase over the total volume of the liquid phase for different Weber numbers and mesh resolutions, as obtained within the Eulerian-Eulerian framework of the multiscale two-fluid approach, namely, the fragment volume over time is calculated based on the

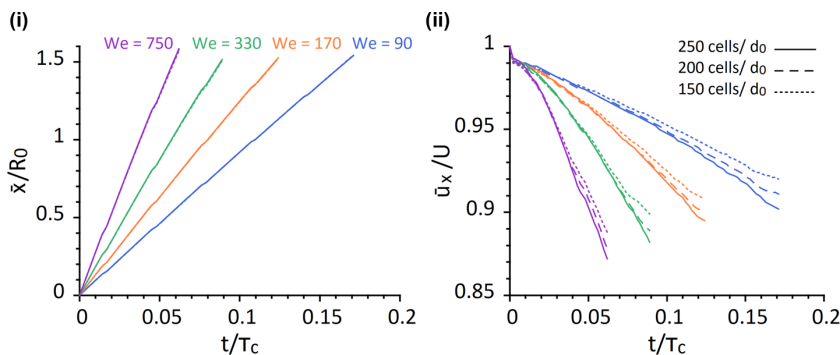


FIG. 14. Center-of-mass properties for a methyl-ethyl-ketone (MEK) droplet at $We = 90, 170, 330,$ and 750 . (i) Position and (ii) velocity of the center-of-mass in the axial direction. Mesh convergence investigation using three different mesh resolutions of 150, 200, and 250 cells per initial droplet diameter.

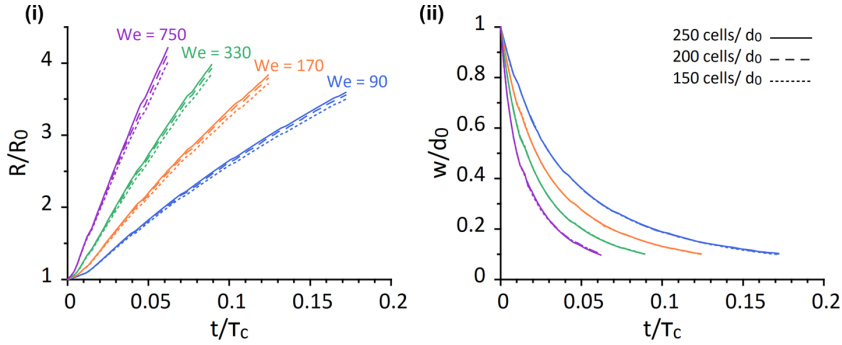


FIG. 15. Evolution of the laser-induced deformation for a methyl-ethyl-ketone (MEK) droplet at $We = 90$, 170, 330, and 750. (i) Droplet radius expansion and (ii) droplet width reduction. Mesh convergence investigation using three different mesh resolutions of 150, 200, and 250 cells per initial droplet diameter.

liquid volume fraction and not on the absolute volume of the detached fragments. As a result, even though the absolute number of fragments is continuously increasing over time, very dilute liquid regions within the cloud of fragments that correspond to significantly low liquid volume fractions and equivalent fragment diameters $< 0.09 \mu\text{m}$ are excluded. This phenomenon is more pronounced at low Weber numbers 90 and 170; here, the fragmentation rate attenuates at the later stages, and significantly less large-scale fragments are detached from the rim, which is depicted as a nonmonotonous concentration of fragments in Fig. 16. Overall, the concentration of dispersed fragments captured within the multiscale framework converges toward the solution obtained with the finest mesh, concerning the initiation of the rim breakup and the progressive detachment of fragments over time. Specifically, at Weber numbers 330 and 750, the intermediate mesh results with a resolution of 200 cells/ d_0 are found to approach more closely the finest mesh solution during the later stages of fragmentation compared with the lower Weber number cases with values 90 and 170. However, at lower Weber numbers, the rim fragmentation is less violent, and the concentration of fragments relatively stabilizes over time. As a result, the deviation between the results for a resolution of 200 and 250 cells/ d_0 is mainly enhanced by new fragments $< 1 \mu\text{m}$. Thus, it is safe to conclude that the calculated concentrations of fragments using the multiscale two-fluid approach satisfactorily converge in all examined conditions.

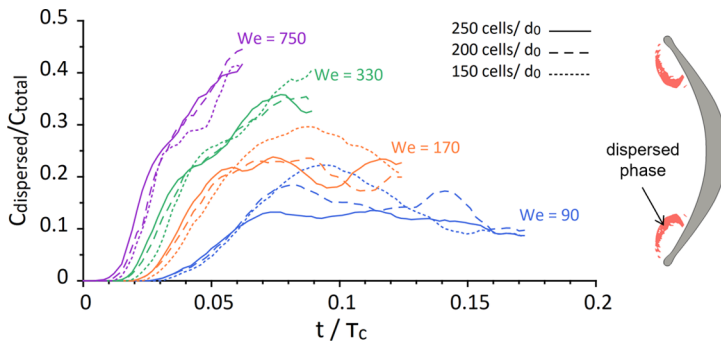


FIG. 16. Evolution of the laser-induced rim fragmentation for a methyl-ethyl-ketone (MEK) droplet at $We = 90$, 170, 330, and 750. Volume concentration of the dispersed phase over the total volume of the liquid phase. Mesh convergence investigation using three different mesh resolutions of 150, 200, and 250 cells per initial droplet diameter.

2. Axisymmetric modeling assumption

An axisymmetric geometry is commonly adopted in numerical simulations of droplet fragmentation cases, as an acceptable compromise between a satisfactory representation of the developed physics and a viable computational cost. Various examples of axisymmetric simulations using a $\sim 5^\circ$ wedge geometry can be found in the literature, such as the explosive fragmentation imposed by a laser-induced cavitation in the study of Zeng *et al.* [22] and the droplet fragmentation due to mechanical impact onto a solid surface with moderate-impact [55,56] and high-impact velocities [31,34].

The laser-induced droplet fragmentation examined here is an unsteady fragmentation process, characterized by two fragmentation modes, namely, the rim and the sheet fragmentation, as identified by Klein *et al.* [25]. In this numerical study, we focus on the investigation of the rim fragmentation simulated until a selected final time before the sheet fragmentation begins. During the rim fragmentation, perturbations with a characteristic wave number form along the rim and evolve into fragments, i.e., ligaments or droplets. The fastest-growing wave number upon the unsteady rim fragmentation for liquids of small viscosity is introduced by Wang *et al.* [57] as follows:

$$k_{\max}^* = \sqrt{\frac{1}{2 + \frac{6\sqrt{2}}{\text{Re}}}}, \quad (\text{B1})$$

where k_{\max}^* is nondimensionalized by the rim diameter b , such that $k_{\max}^* = k_{\max}/(b/2)$. Here, $\tilde{\text{Re}}$ is the local rim Reynolds number which is calculated as follows:

$$\tilde{\text{Re}} = 0.2\text{Oh}^{-5/4}\text{Re}^{-1/4}, \quad (\text{B2})$$

where $\text{Oh} = \mu/\sqrt{\rho\gamma d_0}$ and $\text{Re} = Ud_0/v$ are the Ohnesorge and Reynolds numbers, respectively, for the properties of the initial droplet before fragmentation, i.e., d_0 is the initial droplet diameter, U the propulsion velocity, μ the dynamic viscosity, ρ the density, γ the surface tension, and v the kinematic viscosity.

For the examined MEK droplet at Weber numbers 90, 170, 330, and 750, the fastest-growing wave number obtained from Eq. (B1) is $k_{\max} \cong 0.33b$ in dimensional form. Considering the 5° wedge geometry used and the progressive radial expansion of the droplet, the critical point to examine if the developed wave numbers fit in the utilized wedge geometry is during the initiation of the rim fragmentation process. At this moment, for each examined case, the droplet radius is expanded by $R \cong 1.5R_0$, the azimuthal dimension of the wedge around the rim is $z_{\min} \cong 10^{-4}$ m, and the rim diameter is $b \cong 10^{-4}$ m. As a result, even during the initiation of the rim fragmentation process, the fastest-growing wave number can fit in the 5° wedge geometry since $k_{\max} \cong 0.33 \times 10^{-4} < z_{\min}$. Overall, the axisymmetric 5° wedge geometry is an acceptable modeling compromise in the conducted simulations without suppressing the developed wave numbers and thus influencing the results.

On the contrary, the simulation of the Rayleigh-Taylor instability-driven sheet fragmentation would require not only a 3D geometry but also a significantly high resolution around the extremely thin liquid sheet to accurately resolve the nonaxisymmetric hole nucleation. In practice, this numerical investigation would mean a computationally expensive direct numerical simulation (DNS). However, a computationally efficient simulation within the developed multiscale framework would be possible with a further development of the proposed numerical model to couple an AMR algorithm with the sharp interface formulation. Then the AMR algorithm would provide high resolution around the expanding but still coherent liquid sheet, sufficient to resolve the resulting hole nucleation and, at the same time, operate independently of the subgrid scale modeling for the produced microscale fragments. This model development is beyond the scope of this paper, our numerical study on the laser-induced droplet fragmentation problem, and is part of ongoing research.

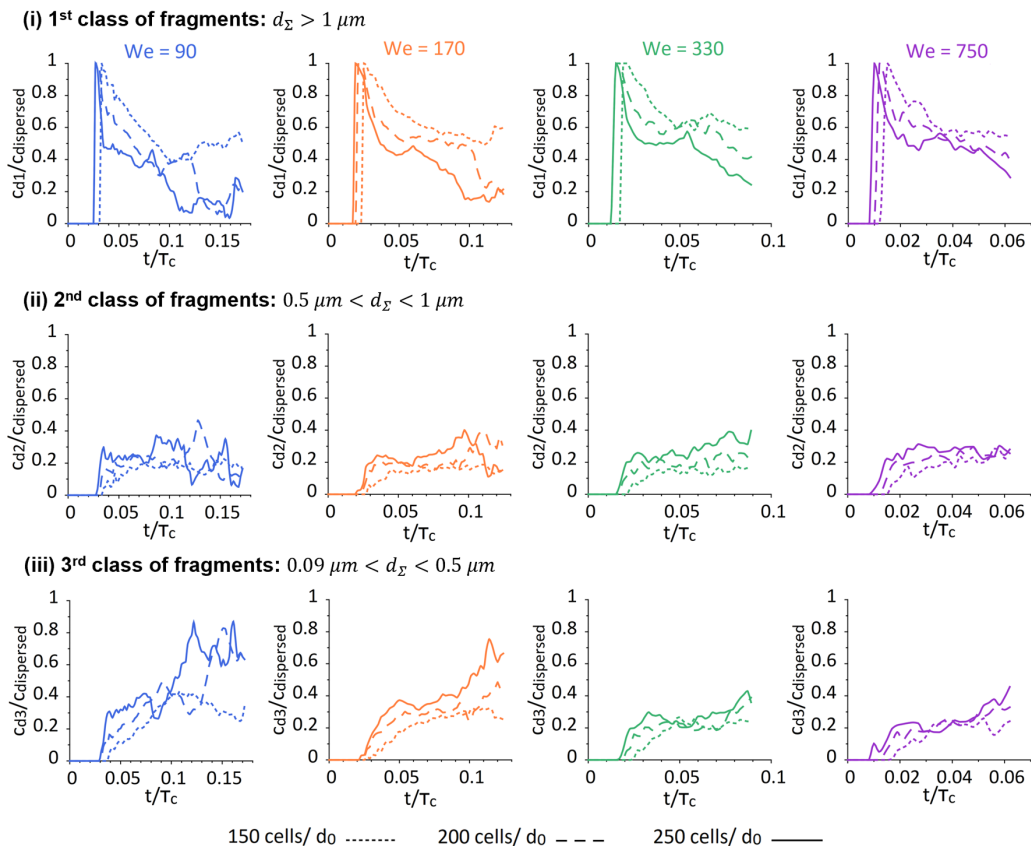


FIG. 17. Volume concentration of three classes of fragments for a methyl-ethyl-ketone (MEK) droplet at $We = 90, 170, 330,$ and 750 over the total volume of the dispersed region, using three different mesh resolutions of 150, 200, and 250 cells per initial droplet diameter.

APPENDIX C: DROPLET SIZE DISTRIBUTIONS: MESH CONVERGENCE INVESTIGATION

The diameter of a subgrid scale fragment is calculated within the multiscale two-fluid approach in Eq. (14) as the equivalent diameter of a spherical particle which has the same volume-to-surface-area ratio as the examined computational cell. Therefore, the fragment diameter is a function of the local calculated interface surface area density and the computational cell volume. In practice, for the same examined computational volume, a very coarse mesh will predict a single large droplet, while a finer mesh will capture the same volume with multiple computational cells and thus will predict a group of smaller droplets, one in each cell. As a result, a coarser mesh enhances the calculation of larger diameters, while in a finer mesh, smaller diameters will dominate. Following this modeling limitation, a moderate mesh resolution is the safest balance to obtain the most accurate representation of the physics and restrict the mesh-related overestimation of larger or smaller droplets.

Considering the inevitable modeling effect of the mesh resolution on the droplet size calculations, the interest of a mesh convergence investigation does not lie in the individual diameter values at a specific time. Instead, the overall evolution of the population of the fragments over time, examining how specific classes of diameters develop upon the rim fragmentation process, is the most significant here. In Fig. 17, the volume concentrations of three classes of fragments, the same as in Fig. 11, with diameters $d_\Sigma > 1 \mu\text{m}$, $0.5 \mu\text{m} < d_\Sigma < 1 \mu\text{m}$, and $0.09 \mu\text{m} < d_\Sigma < 0.5 \mu\text{m}$ are illustrated

for a MEK droplet at $We = 90, 170, 330,$ and 750 over the total volume of the dispersed region, using three different mesh resolutions.

For the highest droplet propulsion velocities with corresponding Weber number values of 330 and 750 , the concentration of droplets over time follows the same tendency in the three presented classes of fragments in Fig. 17, irrespectively of the mesh resolution used. As expected, the largest fragments of the first class are found to be more significant with the coarsest mesh of $150 \text{ cells}/d_0$ even during the later stages of rim fragmentation, while the smaller fragments of the second and third classes are more pronounced with the finest mesh of $250 \text{ cells}/d_0$. For $We = 330$, the droplet size distribution of Fig. 12 is obtained at the final time $0.089 \tau_c$, when the maximum observed deviation between the moderate and the finest mesh results is found for the concentration of the first class of fragments and is $\sim 15\%$. For $We = 750$, the droplet size distribution of Fig. 12 is obtained at $0.062 \tau_c$ with the concentration of the first class of fragments to differ by $< 10\%$ between the mesh of 200 and $250 \text{ cells}/d_0$. Overall, the observed small deviations between the calculated concentrations of different classes of fragments for Weber number values of 330 and 750 do not violate the overall capturing of the phenomenon.

Focusing on the lower propulsion velocities with Weber number values of 90 and 170 and the first class of fragments in Fig. 17(i), the concentration of the largest droplet class is reduced significantly earlier with the finest mesh of $250 \text{ cells}/d_0$. As previously shown in Fig. 16, after $0.06 \tau_c$, the overall concentration of fragments relatively stabilizes; thus, at this time, the fragmentation process decelerates, and less newly formed fragments are detached from the rim. As a result, the developed cloud of fragments is not as varied as previously and mainly consists of droplets $\sim 1 \mu\text{m}$, instead of a group of large droplets well $> 1 \mu\text{m}$ close to the rim that break down into smaller droplets downstream. In this case, the effect of the mesh resolution on the droplet size calculations $\sim 1 \mu\text{m}$ is pronounced; the mesh of $150 \text{ cells}/d_0$ overestimates the first class of droplets, while the mesh of $250 \text{ cells}/d_0$ underestimates their presence in the cloud of fragments. However, for the time instances that the droplet size distributions of Fig. 12 are obtained, the moderate mesh resolution results satisfactorily converge toward the finest mesh solution; for $We = 90$, the maximum deviation is $< 4\%$ for the second class of fragments, while for $We = 170$, the maximum deviation is observed for the third class of fragments and a difference of 18% .

-
- [1] S. Fujioka, M. Shimomura, Y. Shimada, S. Maeda, H. Sakaguchi, Y. Nakai, T. Aota, H. Nishimura, N. Ozaki, A. Sunahara *et al.*, Pure-Tin microdroplets irradiated with double laser pulses for efficient and minimum-mass extreme-ultraviolet light source production, *Appl. Phys. Lett.* **92**, 241502 (2008).
 - [2] H. Mizoguchi, T. Abe, Y. Watanabe, T. Ishihara, T. Ohta, T. Hori, T. Yanagida, H. Nagano, T. Yabu, S. Nagai *et al.*, 100W 1st generation laser-produced plasma light source system for HVM EUV lithography, in *Extreme Ultraviolet (EUV) Lithography II* (SPIE Advanced Lithography, San Jose, 2011), Vol. 7969, p. 796908.
 - [3] V. Y. Banine, K. N. Koshelev, and G. H. P. M. Swinkels, Physical processes in EUV sources for microlithography, *J. Phys. D: Appl. Phys.* **44**, 253001 (2011).
 - [4] A. Pirati, J. van Schoot, K. Troost, R. van Ballegoij, P. Krabbendam, J. Stoeldraijer, E. Loopstra, J. Benschop, J. Finders, H. Meiling *et al.*, The future of EUV lithography: enabling Moore's law in the next decade, in *Extreme Ultraviolet (EUV) Lithography VIII* (SPIE Advanced Lithography, San Jose, 2017), Vol. 10143, p. 101430G.
 - [5] N. Bloembergen, Brief history of laser-induced breakdown, in *Laser-Induced Damage in Optical Materials: 1998* (SPIE, Boulder, 1999), Vol. 3578, pp. 198–200.
 - [6] E. M. Gattass and R. Rafael, Femtosecond laser micromachining in transparent materials, *Nat. Photonics* **2**, 219 (2008).
 - [7] G. Della Valle, R. Osellame, and P. Laporta, Micromachining of photonic devices by femtosecond laser pulses, *J. Opt. A Pure Appl. Opt.* **11**, 049801 (2009).

- [8] M. M. Krasnov, Laser-phakopuncture in the treatment of soft cataracts, *Br. J. Ophthalmol.* **59**, 96 (1975).
- [9] J. T. Walsh, Pulsed laser angioplasty: A paradigm for tissue ablation, in *Optical-Thermal Response of Laser-Irradiated Tissue*, Lasers, Photonics, and Electro-Optics, edited by A. J. Welch and M. J. C. Van Gemert (Springer, Boston, 1995), pp. 865–902.
- [10] A. Vogel and V. Venugopalan, Mechanisms of pulsed laser ablation of biological tissues, *Chem. Rev.* **103**, 577 (2003).
- [11] I. Apitz and A. Vogel, Material ejection in nanosecond Er : YAG laser ablation of water, liver, and skin, *Appl. Phys. A* **81**, 329 (2005).
- [12] S. R. Gonzalez Avila and C. D. Ohl, Fragmentation of acoustically levitating droplets by laser-induced cavitation bubbles, *J. Fluid Mech.* **805**, 551 (2016).
- [13] M. S. Krivokorytov, Q. Zeng, B. V. Lakatosh, A. Y. Vinokhodov, Y. Y. Sidelnikov, V. O. Kompanets, V. M. Krivtsun, K. N. Koshelev, C. D. Ohl, and V. V. Medvedev, Shaping and controlled fragmentation of liquid metal droplets through cavitation, *Sci. Rep.* **8**, 597 (2018).
- [14] P. Kafalas and J. Herrmann, Dynamics and energetics of the explosive vaporization of fog droplets by a 106-mm laser pulse, *Appl. Opt.* **12**, 772 (1973).
- [15] P. Kafalas and A. P. Ferdinand, Fog droplet vaporization and fragmentation by a 106-mm laser pulse, *Appl. Opt.* **12**, 29 (1973).
- [16] V. P. Sandireddy, K. P. Koirala, G. Duscher, and R. Kalyanaraman, Explosive vaporization of metallic nanostructures on a surface by nanosecond laser heating under fluids, *J. Appl. Phys.* **129**, 064901 (2021).
- [17] J.-Z. Zhang, J. K. Lam, C. F. Wood, B.-T. Chu, and R. K. Chang, Explosive vaporization of a large transparent droplet irradiated by a high intensity laser, *Appl. Opt.* **26**, 4731 (1987).
- [18] D. Kurilovich, A. L. Klein, F. Torretti, A. Lassise, R. Hoekstra, W. Ubachs, H. Gelderblom, and O. O. Versolato, Plasma Propulsion of a Metallic Microdroplet and Its Deformation Upon Laser Impact, *Phys. Rev. Appl.* **6**, 014018 (2016).
- [19] R. G. Pinnick, A. Biswas, R. L. Armstrong, S. G. Jennings, J. D. Pendleton, and G. Fernández, Micron-sized droplets irradiated with a pulsed CO₂ laser: measurement of explosion and breakdown thresholds, *Appl. Opt.* **29**, 918 (1990).
- [20] M. M. Basko, M. S. Krivokorytov, A. Yu. Vinokhodov, Y. V. Sidelnikov, V. M. Krivtsun, V. V. Medvedev, D. A. Kim, V. O. Kompanets, A. A. Lash, and K. N. Koshelev, Fragmentation dynamics of liquid-metal droplets under ultra-short laser pulses, *Laser Phys. Lett.* **14**, 36001 (2017).
- [21] S. Y. Grigoryev, B. V. Lakatosh, M. S. Krivokorytov, V. V. Zhakhovsky, S. A. Dyachkov, D. K. Ilnitsky, K. P. Migdal, N. A. Inogamov, A. Y. Vinokhodov, V. O. Kompanets *et al.*, Expansion and Fragmentation of a Liquid-Metal Droplet by a Short Laser Pulse, *Phys. Rev. Appl.* **10**, 064009 (2018).
- [22] Q. Zeng, S. R. Gonzalez-Avila, S. Ten Voorde, and C.-D. Ohl, Jetting of viscous droplets from cavitation-induced Rayleigh-Taylor instability, *J. Fluid Mech.* **846**, 916 (2018).
- [23] A. L. Klein, W. Bouwhuis, C. W. Visser, H. Lhuissier, C. Sun, J. H. Snoeijer, E. Villermaux, D. Lohse, and H. Gelderblom, Drop Shaping by Laser-Pulse Impact, *Phys. Rev. Appl.* **3**, 044018 (2015).
- [24] A. L. Klein, D. Lohse, M. Versluis, and H. Gelderblom, Apparatus to control and visualize the impact of a high-energy laser pulse on a liquid target, *Rev. Sci. Instrum.* **88**, 095102 (2017).
- [25] A. L. Klein, D. Kurilovich, H. Lhuissier, O. O. Versolato, D. Lohse, E. Villermaux, and H. Gelderblom, Drop fragmentation by laser-pulse impact, *J. Fluid Mech.* **893**, A7 (2020).
- [26] E. Villermaux, Fragmentation, *Ann. Rev. Fluid Mech.* **39**, 419 (2007).
- [27] D. C. K. Rao, A. P. Singh, and S. Basu, Laser-induced deformation and fragmentation of droplets in an array, *Int. J. Multiph. Flow* **148**, 103925 (2022).
- [28] P. Koukouvinis, N. Kyriazis, and M. Gavaises, Smoothed particle hydrodynamics simulation of a laser pulse impact onto a liquid metal droplet, *PLoS One* **13**, e0204125 (2018).
- [29] D. R. Guildenbecher, C. Lopez-Rivera, and P. E. Sojka, Secondary atomization, *Exp. Fluids* **46**, 371 (2009).
- [30] Z. Wu and Y. Cao, Dynamics of initial drop splashing on a dry smooth surface, *PLoS One* **12**, e0177390 (2017).
- [31] G. Tretola and K. Vogiatzaki, Numerical treatment of the interface in two phase flows using a compressible framework in OpenFOAM: demonstration on a high velocity droplet impact case, *Fluids* **6**, 78 (2021).

- [32] H. Gelderblom, H. Lhuissier, A. L. Klein, W. Bouwhuis, D. Lohse, E. Villermaux, and J. H. Snoeijer, Drop deformation by laser-pulse impact, *J. Fluid Mech.* **794**, 676 (2016).
- [33] S. A. Reijers, J. H. Snoeijer, and H. Gelderblom, Droplet deformation by short laser-induced pressure pulses, *J. Fluid Mech.* **828**, 374 (2017).
- [34] G. Nykteri, P. Koukouvinis, R. S. Gonzalez Avila, C.-D. Ohl, and M. Gavaises, A Σ -Y two-fluid model with dynamic local topology detection: application to high-speed droplet impact, *J. Comput. Phys.* **408**, 109225 (2020).
- [35] C. W. Hirt and B. D. Nichols, Volume of fluid (VOF) method for the dynamics of free boundaries, *J. Comput. Phys.* **39**, 201 (1981).
- [36] R. Scardovelli and S. Zaleski, Direct numerical simulation of free-surface and interfacial flow, *Annu. Rev. Fluid Mech.* **31**, 567 (1999).
- [37] A. Vallet and R. Borghi, Modelisation eulerienne de l'atomisation d'un jet liquide, *C. R. Acad. Sci. IIB* **327**, 1015 (1999).
- [38] R. Lebas, T. Menard, P. A. Beau, A. Berlemont, and F. X. Demoulin, Numerical simulation of primary break-up and atomization: DNS and modelling study, *Int. J. Multiph. Flow* **35**, 247 (2009).
- [39] M. Ishii and K. Mishima, Two-Fluid model and hydrodynamic constitutive relations, *Nucl. Eng. Des.* **82**, 107 (1984).
- [40] J. Boussinesq, *Essai sur la théorie des eaux courantes: Mémoires présentés par divers savants à l'Académie des sciences de l'Institut national de France* (Impr. nationale, Paris, 1877).
- [41] J. U. Brackbill, D. B. Kothe, and C. Zemach, A continuum method for modeling surface tension, *J. Comput. Phys.* **100**, 335 (1992).
- [42] G. I. Kelbaliyev, Drag coefficients of variously shaped solid particles, drops, and bubbles, *Theor. Found. Chem. Eng.* **45**, 248 (2011).
- [43] A. Vallet, A. A. Burluka, and R. Borghi, Development of a Eulerian model for the "atomization" of a liquid jet, *At. Sprays* **11**, 619 (2001).
- [44] A. Andreini, C. Bianchini, S. Puggelli, and F. X. Demoulin, Development of a turbulent liquid flux model for Eulerian-Eulerian multiphase flow simulations, *Int. J. Multiph. Flow* **81**, 88 (2016).
- [45] J. Chesnel, J. Reveillon, T. Menard, and F. X. Demoulin, Large eddy simulation of liquid jet atomization, *At. Sprays* **21**, 711 (2011).
- [46] G. Nykteri and M. Gavaises, Droplet aerobreakup under the shear-induced entrainment regime using a multiscale two-fluid approach, *Phys. Rev. Fluids* **6**, 084304 (2021).
- [47] M. J. Iivings, D. M. Causon, and E. F. Toro, On Riemann solvers for compressible liquids, *Int. J. Numer. Methods Fluids* **28**, 395 (1998).
- [48] R. T. Lahey, The simulation of multidimensional multiphase flows, *Nucl. Eng. Des.* **235**, 1043 (2005).
- [49] S. Karthika, T. K. Radhakrishnan, and P. Kalaichelvi, A review of classical and nonclassical nucleation theories, *Cryst. Growth Des.* **16**, 6663 (2016).
- [50] E. Villermaux and B. Bossa, Drop fragmentation on impact, *J. Fluid Mech.* **668**, 412 (2011).
- [51] V. S. Jagadale, D. C. K. Rao, D. Deshmukh, D. Hanstorp, and Y. N. Mishra, Modes of atomization in biofuel droplets induced by a focused laser pulse, *Fuel* **315**, 123190 (2022).
- [52] P. Sopena, J. M. Fernández-Pradas, and P. Serra, Laser-induced forward transfer of conductive screen-printing inks, *Appl. Surf. Sci.* **507**, 145047 (2020).
- [53] J. Zhou and M. Andersson, Break-up induced by the collapse of laser-generated cavitation bubbles in a liquid jet, in *14th Triennial International Conference on Liquid Atomization and Spray Systems* (ICLASS, Chicago, 2018).
- [54] P. Rohilla and J. Marston, Feasibility of laser induced jets in needle free jet injections, *Int. J. Pharm.* **589**, 119714 (2020).
- [55] Y. Guo, Y. Lian, and M. Sussman, Investigation of drop impact on dry and wet surfaces with consideration of surrounding air, *Phys. Fluids* **28**, 073303 (2016).
- [56] N. Kyriazis, P. Koukouvinis, and M. Gavaises, Modelling cavitation during drop impact on solid surfaces, *Adv. Colloid Interface Sci.* **260**, 46 (2018).
- [57] Y. Wang, R. Dandekar, N. Bustos, S. Poulain, and L. Bourouiba, Universal Rim Thickness in Unsteady Sheet Fragmentation, *Phys. Rev. Lett.* **120**, 204503 (2018).